# Noise Evaluation of a Digital Neutron Imaging Device

UNDEGRADUATE HONORS THESIS

Presented in Partial Fulfillment of the Requirements for Graduation with Honors Research Distinction in the Department of Mechanical Engineering of The Ohio State University

By

Radoslaw Lewandowski

Undergraduate Program in Mechanical Engineering

The Ohio State University

2012

Defense Committee:

Lei Cao, Ph.D., Advisor

Chia-Hsiang Menq, Ph.D.

## Abstract

Radiography consists of methods aimed at providing a nondestructive mean of imaging internal structures and composition of matter by recording the transmitted intensity of a beam of radiation. The enormous popularity of X-ray imaging in medicine has driven an effort in X-ray radiography aimed at standardizing and regulating the acquisition of X-ray radiographs and quantifying image quality across different X-ray platforms. However, a similar discussion has not been observed in neutron radiography (NR), a type of imaging technique that uses neutrons as a source of radiation. Currently, the Modulation Transfer Function (MTF) is solely used to measure the quality of NR systems. However, MTF is a measure of contrast only and does not account for noise. The purpose of this research was to take additional metrics including the Noise Power Spectrum (NPS) and the Detective Quantum Efficiency (DQE) that are commonly used in X-ray imaging, apply them to NR, and evaluate the impact of noise. An imaging system was developed using a low-cost digital camera, modified with open source software to enhance imaging capabilities. The system allowed capturing images of a neutron beam produced by the OSU Research Reactor at various exposure times. The produced images were analyzed with the help of MATLAB to establish MTF, NPS, and DQE measurements. The results confirmed the initial hypothesis by showing that although a system may have very high contrast, it may suffer from noise, which

deteriorates the system's ability to detect fine details. The results and discussion presented here have been published in a journal in hope to inform the NR community of the nuisances associated with noise and suggest that NPS and DQE are used to complement MTF in an attempt to describe the quality of neutron imaging devices.

Acknowledgments

I would like to thank my advisor, Dr. Lei Cao, for the guidance and insight provided throughout the course of this project and Danyal Turkoglu for his help and assistance in data collection and analysis. I also want to thank Andrew Kauffman, Kevin Herminghuysen, and Joseph Talnagi at the OSU Research Reactor.

# Vita

June 2008 ..... North Royalton High School

2012 ..... B.S. Mechanical Engineering, The Ohio State University

## Publications

Radoslaw Lewandowski, Lei Cao*, Danyal Turkoglu. "*Noise Evaluation of a Digital Neutron Imaging Device.*" Nuclear Inst. and Methods in Physics Research, A. 674, (2012): 46–50.

Turkoglu, D., Lewandowski, Radoslaw, Cao, Lei, "*A Low-cost Neutron Radiography Device and the Discussion of MTF and DQE."* IEEE Transactions on Nuclear Science, 2012. Submitted.

## Fields of Study

Major Field: Mechanical Engineering

Table of Contents

List of Tables

List of Figures

# Chapter 1: Introduction

## 1.1. Background

*Radiography* consists of a range of methods aimed at providing a nondestructive mean of imaging internal structures and composition of matter by recording the transmitted intensity of a beam of radiation. It was an almost immediate consequence following the discovery of penetrative properties of radiation and continues to be a significant application of such sources today. The most common type of radiography uses *X-rays* as a source of radiation widely applied in *radiology*, a medical field utilizing imaging to diagnose and treat illnesses present in a human body. However, other sources of radiation including high-energy *gamma rays* from radioisotope sources, high-energy *bremsstrahlung* from electron linear accelerators and *neutrons* are also used to produce radiographic images [1].

Following Chadwick's discovery of neutrons in 1932, Kallmann and Kuhn performed first experiments in *neutron radiography (NR)* as early as 1935. These experiments used a small accelerator neutron source and resulted in low quality radiographs that required long development times [2]. Peter was able to produce images of a higher quality in a shorter time frame using a more intense neutron source. However, work in neutron radiography was suspended during World War II and then revisited in mid-1950s. Several groups including Berger, Watts, Barton, Criscuolo and Polansky,

Shultz and Leavitt established neutron radiography as a nondestructive inspection method in the 1960s [2]. However, this renewed interest in neutron radiography and a growing number of researchers conducting their own experiments called for a standardization of the field. In 1981, the Neutron Radiography Working Group, formed by The Commission of European Communities, and researchers in the United States and Canada developed the Neutron Radiography Handbook. The Handbook served as a reference delineating standard procedures for acquiring neutron radiographs [2]. Developments in the 1980s and 1990s gave rise to numerous applications of neutron radiography such as imaging water flow in fuel cells [3], detection of drugs and explosives [4], and revealing illicitly smuggled special materials [5, 6].

### 1.2. Comparison with X-ray Radiography

Because of the likelihood that the general audience is familiar with X-ray imaging and its regular application in medical examinations, it is helpful to compare and contrast neutron radiography with X-ray radiography. As the name indicates, X-ray radiography uses sources emitting electromagnetic waves that interact with target material. More specifically, the incident photons interact with the electronic shells of the atoms and cause emission of secondary electrons that are then recorded [1]. The probability of photon absorption increases with increasing *atomic number, Z,* of the absorber material. Consequently, X-ray radiography cannot be used to image light elements because their attenuation of X-rays is insufficient. In contrast, in neutron radiography a beam of neutrons is used to penetrate a target material. The incident neutrons interact with the

atom's nucleus rather than its electron cloud. The probability of neutron absorption by the target material is independent of the material's atomic number. This probability is random and can vary even among different isotopes of the same element [7]. Furthermore, several light elements such as hydrogen, boron, and lithium are good neutron absorbers, whereas a number of heavy materials including lead and titanium are weak neutron attenuators [7]. To help explain this concept, Figure 1 shows a graphical comparison between X-ray absorption cross sections and neutron absorption cross section of several elements. The actual cross sections, determined using [8] and [9] are listed in Table 1.

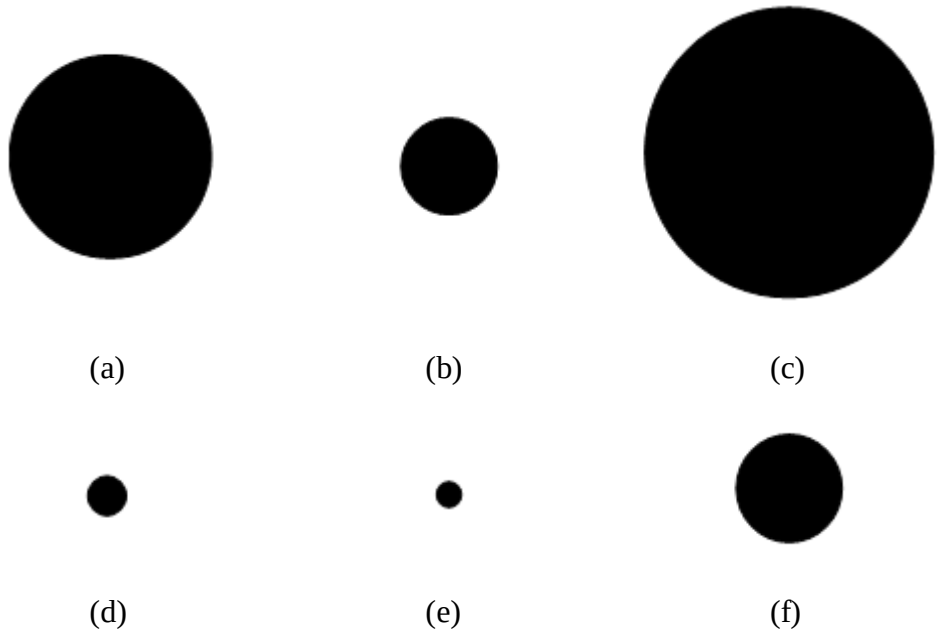


Figure 1: Comparison between absorption cross sections. Neutron absorption cross sections are shown for (a) B, (b) Li, and (c) Gd. X-ray absorption cross section are shown for (d) B, (e) Li, and (f) Gd.

Table 1: Neutron and X-ray absorption cross section for B, Li, and Gd.

| Element | Neutron absorption cross section (barns) | X-ray absorption cross section (barns) |
|---|---|---|
| B | 760 | 1.86 |
| Li | 71 | 1.14 |
| Gd | $49\times10^{3}$ | 88.62 |

As a result, neutron radiography has been applied in a range of applications where X-ray imaging proves insufficient. However, neutron radiography and X-ray radiography are to be treated as complementary examination methods rather than substitutes. To help visualize the importance of these imaging properties, Figure 2 shows an example of a cigarette case examined with X-rays and neutrons [7]. Clearly, the two radiographs of the cigarette case vary due to the neutron and X-ray absorption probabilities of the materials contained in the cigarette case.

Figure 2: An image of a cigarette case obtained using (from left to right): a regular camera, neutrons, and X-rays (adapted from [7]).

## 1.3. Research Objectives

The enormous popularity of X-ray imaging in medicine has driven an effort in X-ray radiography aimed at standardizing and regulating the acquisition of X-ray radiographs and quantifying image quality across different X-ray platforms. Several tools used to determine image quality include the Modulation Transfer Function (MTF), the Noise Power Spectrum (NPS), and the Detective Quantum Efficiency (DQE). However, these metrics have not been readily applied to neutron radiography. More specifically, the neutron radiography field has not witnessed a conversation focused on noise evaluation that is visible in X-ray radiography.

In addition, present-day neutron radiography systems often use expensive, cryogenically cooled, and highly specialized CCD cameras. Nevertheless, an off-the-shelf digital camera may prove to be a low-cost alternative providing sufficient resolution and detection of details. It is, however, important to provide metrics capable of quantifying the imaging abilities of such camera. An experiment was designed to test the validity of using a low-cost camera in a neutron imaging system and quantify its performance. To summarize, the objectives of this research experiment were to:

1) Test a low-cost off-the-shelf digital camera in an in-house developed neutron imaging system
2) Apply the Modulation Transfer Function, the Noise Power Spectrum and the Detective Quantum Efficiency to neutron radiography

3) Examine the impact of fluence on the quality and noise of the in-house developed neutron imaging system.

The acquired experimental results led to an in-depth analysis and subsequent conclusions. The thesis consists of five chapters. Chapter 2 presents the theoretical concepts behind the performance metrics used in evaluating the neutron imaging system. Chapter 3 outlines the experimental procedure applied in acquiring neutron radiographs. Chapter 4 discusses the results and offers their interpretation in light of noise evaluation. Finally, Chapter 5 summarizes the key findings of this thesis, examines additional applications of the presented research, and points towards future studies related to this topic.

# Chapter 2: Performance Evaluation Metrics

## 2.1. Modulation Transfer Function (MTF)

### 2.1.1. Definition

The *Modulation Transfer Function* is a popular tool within optical engineering and photography used to characterize a system's or a component's contrast. The contrast here is defined as the ratio of output modulation to an input sinusoidal modulation with varying *spatial frequency* [10]. Alternatively, MTF can be described as the spatial frequency response of an imaging system. MTF measures contrast at a given spatial frequency relative to low frequencies [11]. Spatial frequency corresponds to the number of cycles (line pairs) per unit distance (usually measured in millimeters or inches). This unit is the result of the two-dimensional nature of the output. High spatial frequencies imply sharp transient of contrast. However, all digital cameras and lenses are inherently low-pass filters [11]. In other words, the detecting systems transmit inputs at low frequencies while attenuating high frequency content. In a sense, imaging systems are analogous to sound systems. A sound recording is a one-dimensional response of a system that can be decomposed into its amplitude and frequency content.

Table 2 compares imaging and sound systems.

Table 2: Comparison between Sound and Imaging Systems

| | Sound System | Imaging System |
|---|---|---|
| Dimensional Regime | One-dimensional | Two-dimensional |
| Domain | Time domain | Spatial Domain |
| Frequency Units | Hertz (Hz, $s^{-1}$) | Cycles (line pairs) per distance (lp/mm, lp/inch, cycles/mm, cycles/inch) |

Another common way to quantify contrast uses Michelson's formula shown in (1) [12]. Here, $I_{max}$ and $I_{min}$ respectively represent the maximum and minimum intensity visible in an image. Michelson contrast, however, does not provide information about spatial correlation present in an image.

$$C = \frac{I_{max} - I_{min}}{I_{max} + I_{min}} \quad (1)$$

2.1.2. Edge Spread Function (ESF)

To determine the MTF curve of an imaging system, an image of a sharp *edge*, made out of highly neutron absorbing material, must be obtained first. The edge serves as a step input to the system. An image is represented by an array of pixel values. However, intensities of pixel values are of interest here rather than the differences in colors. Thus, when using a color digital camera, the image is converted from a RGB scale (Red-Green-Blue) to a grayscale. A *region of interest* (ROI) that is approximately evenly divided between the background space and the edge is depicted in Figure 3.

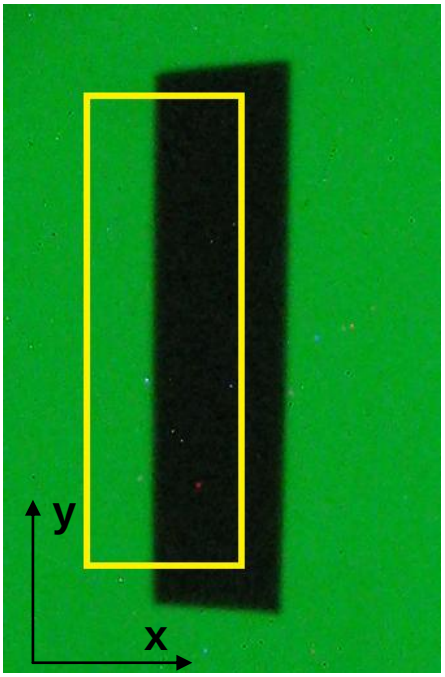


Figure 3: A neutron image of a sharp edge made out of gadolinium before conversion to grayscale. The gadolinium strip is shown as a dark rectangular object. The yellow rectangle outlines the ROI. The green background is a result of the green light emitted by the scintillation screen.

The *Edge Spread Function* represents the averaged pixel intensity values along the x-axis corresponding to Figure 3. Thus, ESF provides insight on how the imaging system treats edges [13]. Under ideal conditions where the edge is perfectly straight and no blurring occurs in the imaging mechanism, ESF would take a shape of an ideal step function.

2.1.3. Line Spread Function (LSF) and Calculation of MTF

The *Line Spread Function* represents the probability density function of locating the edge in the output image [13]. It is determined by differentiating ESF according to (2).

$$LSF(x) = \frac{d(ESF)}{dx} \tag{2}$$

Due to the number array representation of images and ESF, LSF is determined using numerical methods. A system with a perfect resolution would result in an LSF curve represented by a Dirac delta function [13].

The MTF curve is obtained by applying the Fourier transform to LSF as shown in (3). MTF is usually normalized by its magnitude at a spatial frequency of 0. In other words, MTF values at specific spatial frequencies are typically denoted as a percentage. A constant equal to 1 would represent the MTF curve of an ideal system.

$$MTF(f) = FFT\{LSF(x)\} \tag{3}$$

The spatial frequency corresponding to MTF = 10% (10MTF) is often used to determine the effective spatial resolution limit ($R_l$) described in (4).

$$R_l = \frac{1}{2 \times MTF10} \tag{4}$$

## 2.2. Noise Power Spectrum (NPS)

### 2.2.1. Definition

MTF is a measure of contrast only and does not account for the noise experienced by the imaging system. For instance, a system can produce images with a very high contrast, but also degrade the quality by introducing high levels of noise. For this purpose, the *Noise Power Spectrum* is used to quantify the power of noise and its relation to spatial frequency.

Noise is viewed as deviations from the true input signal. In the field of radiography, it is defined as fluctuations from the expected value of a stochastic process [14]. However, it is important to note the difference between noise and interference. Figliola and Beasley define interference as undesirable deterministic trends on the measured value [15]. Furthermore, they define noise strictly as a deviation from the measured value resulting from variation of the extraneous variables [15]. The inability of a system to discern between noise and a true value contributes to the system's random error and uncertainty in accuracy of the results. A short discussion of noise and its adherence to the statistical Poisson distribution is provided in Workman [16].

### 2.2.2. Mathematical Interpretation

NPS is calculated by acquiring a radiograph of a background and translating it into the spatial frequency spectrum using the Fourier transform. The International Standard IEC 62220-1 used in X-ray imaging was adapted for a neutron imaging experiment performed as a part of this research. The same standard defines NPS as the Fourier transform of auto-correlation of noise [14]. Eq. (5) provides the mathematical representation of NPS.

$$NPS(u_n, v_k) = \lim_{M,N_x,N_y \to \infty} \frac{\Delta x \Delta y}{M \times N_x \times N_y} \times \sum_{m=1}^{M} \left| \sum_{i=1}^{N_x} \sum_{j=1}^{N_y} \left[ I(x_i, y_j) - S(x_i, y_j) \right] e^{\left(-2\pi i (u_n x_i + v_k y_j)\right)} \right|^2 \quad (5)$$

According to (5), a grayscale radiographic output consists of $M$ regions of interests, where each ROI is a matrix of $N_x$ by $N_y$ elements, or pixels. Each pixel position within a ROI is identified by Cartesian coordinates $(x_i, y_j)$ and its grayscale intensity, or value is denoted by $I(x_i,y_j)$. In addition, for each ROI, a two-dimensional polynomial $S$ is fitted to determine the mean of the region. Since noise serves as the foundation of NPS, it is important to examine only the noise level present in the signal. Consequently, the 2-D Fourier transform is applied to each ROI corrected for the mean trend, $I(x_i,y_j)-S(x_i,y_j)$, and then squared. The resulting sum of squared Fourier transform amplitudes must be divided by $M$ to achieve a representative result for an average ROI. Furthermore, the results of the average ROI must be multiplied by the pixel size (where $\Delta x$ and $\Delta y$ are pixel width and height in the $i$ and $j$ directions, respectively) and then normalized by the number of pixels in the ROI ($N_x$ and $N_y$ that correspond to number of pixels in the $i$ and $j$ directions). If assumed that pixel size was determined in millimeters, it can be stated that the NPS is measured in units of squared millimeters ($mm^2$). Similar to MTF, NPS is a function of spatial frequency (cycles/mm or lp/mm).

### 2.2.3. Physical Interpretation

After a mathematical treatment of NPS, it is crucial to consider its physical meaning. NPS can be alternatively defined as the measure of variance of image intensity described in the spatial frequency spectrum. It is worthwhile to consider a theoretical NPS curve of a noise described by the Poisson distribution with a mean of 1000 shown in Figure 4. It can be inferred that this NPS appears approximately constant and independent

of spatial frequency. Thus, if one were to assume Poisson noise distribution of neutrons entering a radiography system, a constant-shaped NPS such as the one in Figure 4 would be expected. The NPS curves of actual radiographs obtained from the experiment are described in the Results and Discussion section. Any deviations from this theoretical result and a possible explanation are discussed as well.

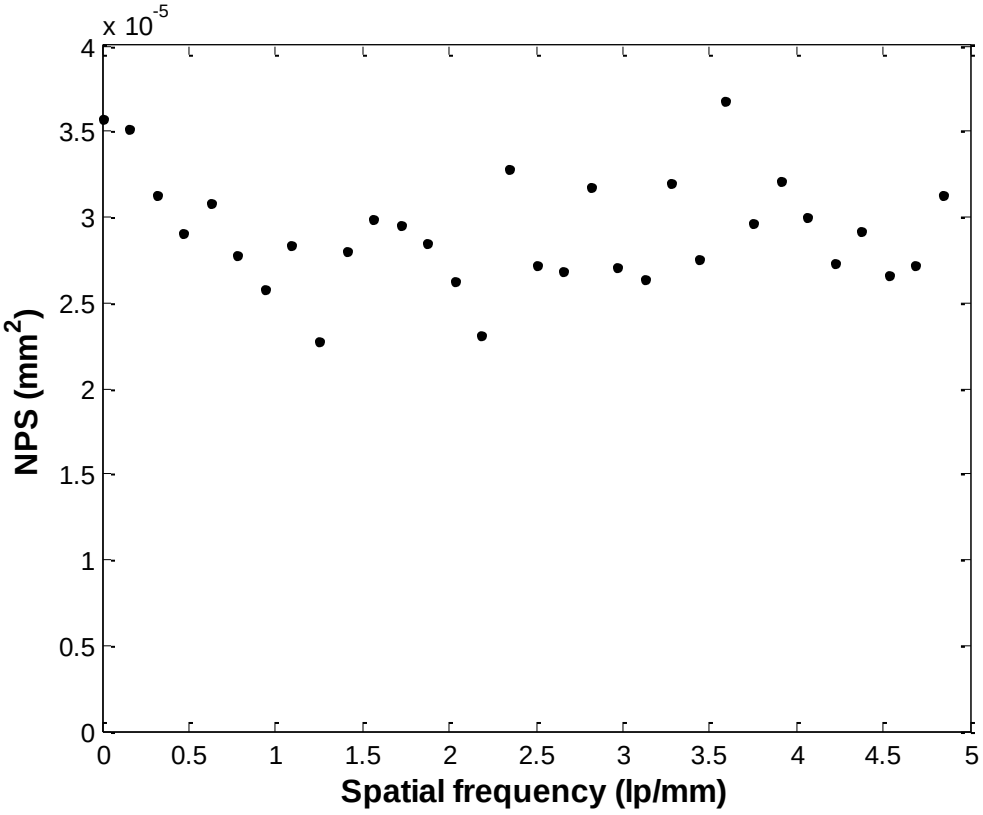


Figure 4: NPS of a Poisson noise distribution with a mean of 1000. The graph suggests a constant NPS value of $3.0 \times 10^{-5}$ $mm^2$ across all spatial frequencies.

## 2.3. Detective Quantum Efficiency (DQE)

### 2.3.1. Signal-to-Noise Ratio (SNR)

An imaging system can be viewed as a black box with input and output *signal-to-noise ratio* as shown in Figure 5. In the case of neutron radiography, neutrons entering the black box serve as the input, while the radiographic image consisting of pixel intensity values acts as an output.

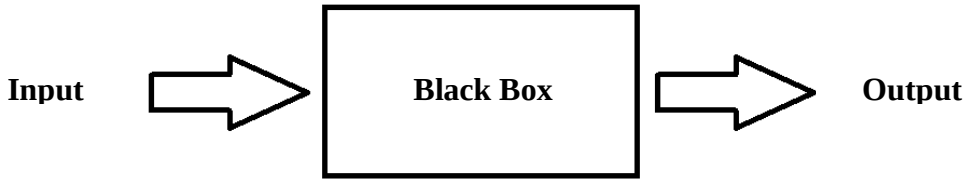


Figure 5: Black Box representation of a neutron imaging device. The incident neutrons enter the imaging device, which then produces a radiographic output.

Furthermore, a Poisson distribution governs the neutrons entering the black box. Therefore, based on counting statistics, the *SNR at the input* is described by:

$$SNR_{input} = \frac{N}{\sigma_N} = \frac{N}{\sqrt{N}} = \sqrt{N} \tag{6}$$

where N is the number of incident neutrons and $\sigma_N$ is their standard deviation. Clearly, the input SNR, also known as the photon or quantum noise, is solely determined by the strength of the source or the exposure time and is independent of the imaging device. On the other hand, (7) defines the *output SNR* as:

$$SNR_{output} = \frac{\overline{P}}{\sigma_{\overline{P}}} \tag{7}$$

where $\overline{P}$ is the mean pixel value and $\sigma_{\overline{P}}$ is the standard deviation of the pixel values. Under ideal conditions, in the absence of noise contributions from the detector, a one-to-one correspondence between an incident neutron and a recorded pixel value is expected, resulting in output SNR equal to input SNR. However, signal loss and noise gain in an actual detector deteriorate the output SNR, which causes the output SNR to be less than input SNR.

### 2.3.2. Noise Equivalent Quanta (NEQ) and DQE

If assuming that an imaging system serves as an ideal counter, then the number of incident neutrons required to produce an image of a specified quality can be derived from the output SNR. This quantity, known as the *Noise Equivalent Quanta*, is expressed in (8) [17].

$$NEQ = \left(SNR_{output}\right)^2 \tag{8}$$

The definition of NEQ and (6) allow representing the *Detective Quantum Efficiency* in the form of (9) [17].

$$DQE = \frac{\left(SNR_{output}\right)^2}{\left(SNR_{input}\right)^2} = \frac{NEQ}{N} \tag{9}$$

Thus, DQE is a ratio that describes the efficiency of the system in utilizing the incident neutrons to produce an output with a desired SNR. In an ideal system, the input and output SNR would be equal. Consequently, DQE ranges from 0 to 1.

2.3.3. DQE in the Frequency Domain

It is useful to represent DQE in the frequency domain [18]. To accomplish this, Dobbins represented NEQ as a ratio of MTF to NPS at a given frequency, *f*, as shown in (10) [19].

$$NEQ(f) = \left(SNR_{output}\right)^2 = \frac{MTF^2(f)}{NPS(f)/\left(\overline{P}\right)^2} \tag{10}$$

Here, NPS is normalized by the square of the mean pixel value of the output image. Furthermore, by inserting (10) into (9), (11) is obtained.

$$DQE(f) = \frac{\left(\overline{P}\right)^2 * MTF^2(f)}{NPS(f) * N} \tag{11}$$

Eq. (11) can now be used to evaluate a high-resolution neutron radiography system.

# Chapter 3: The Neutron Imaging Experiment

## 3.1. General Considerations

The Nuclear Analysis and Radiation Sensor (NARS) Laboratory has prepared an imaging device using a low-cost digital camera to capture neutron images and fulfill the objectives set forth in Chapter 1. The device was tested at The Ohio State University Research Reactor (OSURR) during two separate experiments. The goal of the first experiment was to quantify the noise present in the system and show the insufficiency of using MTF as the only metric to describe the quality of produced radiographs. The focus of the second experiment was to describe the performance of the in-house developed system and present it as a low-cost alternative to the cooled CCD cameras that provides a quick access to neutron radiography in applications where such ability is needed but resources are limited.

## 3.2. Description of the Neutron Source

A thermal neutron beam facility, built by Mr. Danyal Turkoglu, Mr. Padhraic Mulligan, and Prof. Lei Cao at the OSURR in 2011[20], produced a source of neutrons required for neutron imaging. The facility contains a neutron collimator placed in Beam Port #2 at an angle of 30° to the reactor core. Figure 6 shows a schematic representation of the OSURR core [20]. The collimator consists of an aluminum tube that encloses

polycrystalline bismuth and single-crystal sapphire. The polycrystalline bismuth serves as a gamma ray filter, while the single-crystal sapphire filters fast neutrons. The beam of neutrons is collimated by a series of parallel apertures made of borated aluminum and lead. In short, a beam of radiation enters the neutron collimator, which then filters its contents and allows only thermal neutrons travelling parallel to the collimator and down the centerline to be delivered to the imaging apparatus. Table 3 lists important neutron beam parameters pertaining to this study. Turkoglu et al. provides a full description of the thermal neutron beam facility in [20].

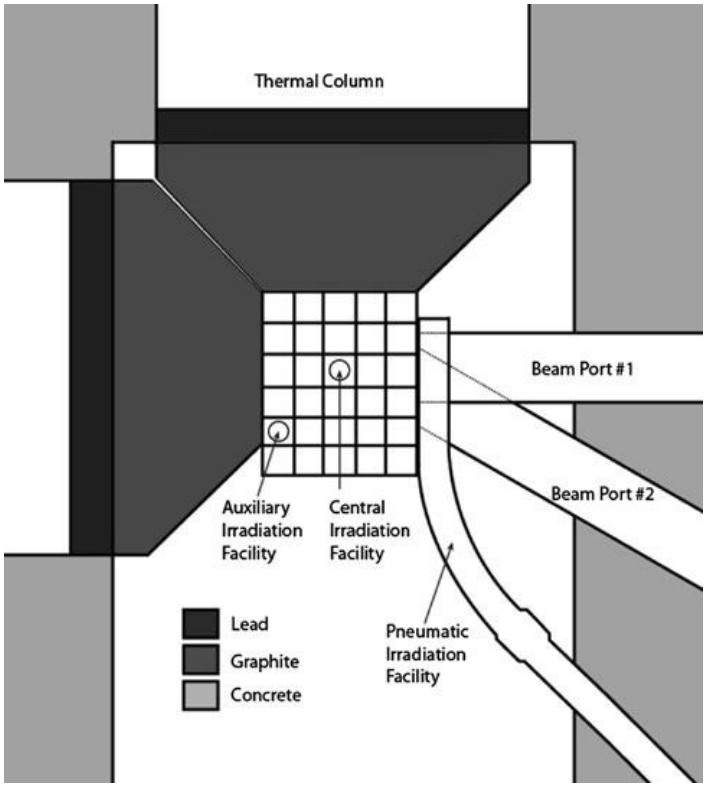


Figure 6: Schematic representation of the OSURR (adapted from [20]).

Table 3: Characteristics of the neutron beam used in the experiment

| Parameter | Value |
|---|---|
| Central uniform part of the beam | ~3 cm |
| Beam divergence | ~2.8° |
| L/D ratio | ~50 |
| Thermal equivalent flux at sample position with 450 kW | $(8.55 \pm 0.19) \times 10^6$ $cm^{-2}s^{-1}$ |
| Cadmium ratio | 266 ± 13 |

3.3. Neutron Imaging System

The NR apparatus consists of an aluminum light-tight box that houses a front-surface mirror, a scintillation screen, and an off-the-shelf digital camera. Table 4 provides a brief summary characterizing the imaging apparatus. A top view of the apparatus is shown in Figure 7.

Table 4: Properties of the neutron imaging system

| | |
|---|---|
| Conversion screen | $^6$LiF/ZnS doped with Cu, Al and Ag blend<br>540 nm (green) light emission<br>0.3 mm thick screen<br>Minimum resolution of 80 µm |
| Mirror | Front-surface soda-lime glass |
| Detecting element | Canon™ SD1100 IS (IXUS 80) |
| Image sensor | 1/2.5 inch type CCD |
| Number of effective pixels | 2448 (V) × 3264 (H)<br>(~8.0 Megapixels) |
| Available shutter times (s) | 1/100,000, …, 1, …, 8, 10, 12.7, 16, 20, 25.4, 32, 40.3, 50.8, 64, 80, 101, 128, …, 2048 |


Figure 7: Top view of the imaging apparatus (adapted from [21]).

Furthermore, Figure 8 shows a schematic representation of the neutron imaging process. The neutron beam emitted from the exit port of the neutron collimator interacts with the scintillation screen placed in its path. A screen developed by the Applied Scintillation Technologies™ (AST), made out of $^{6}$LiF/ZnS and doped with a blend of Cu, Al, and Ag, was used in the experiment. Neutrons, due to lack of charge, cannot be directly measured using principles related to Coulomb's law and ionizing radiation. During a process known as fluorescence, a scintillation screen acts as a conversion material, where the incident neutrons interact with the screen material and emit photons with wavelengths that fall within the visible light spectrum [1]. The light sensor of the digital camera detects and records the resulting light and its intensity. Since it is important to eliminate the contributions from the background light, the scintillation screen and the digital camera are housed in an aluminum light-tight box.

Although the purpose of the neutron collimator is to transmit only thermal neutrons, it is likely that some unattenuated gammas and fast neutrons are still present in the neutron beam. Therefore, to protect the digital camera from incident radiation and possible damage, the aluminum light tight box is constructed with a front-surface aluminized and doped with $^{6}$Li mirror positioned at a 45° angle with respect to the beam. The mirror reflects the light emitted by the scintillation screen towards the camera and absorbs remaining gammas and fast neutrons present in the beam. This allows the camera to be positioned outside of the beam's path and protects it from radiation damage.

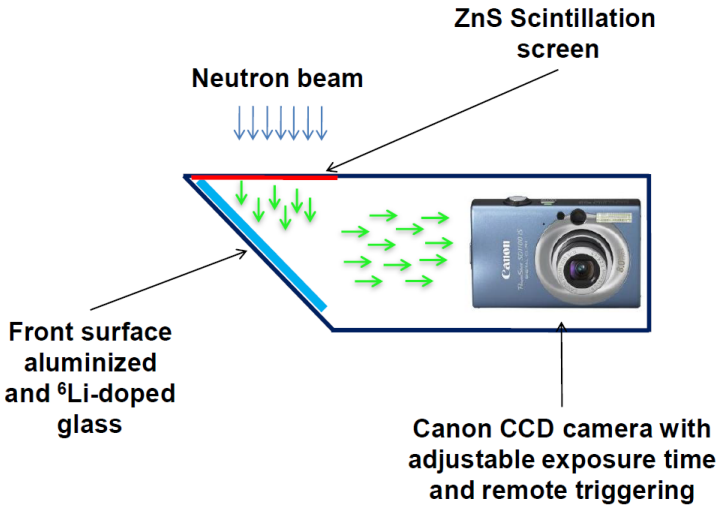


Figure 8: Schematic representation of the neutron imaging process (adapted from [10]).

During the experiment, the imaging apparatus was positioned near the exit port of the beam shutter as shown in Figure 9. The scintillation screen was located approximately 282 cm away from the OSURR core.

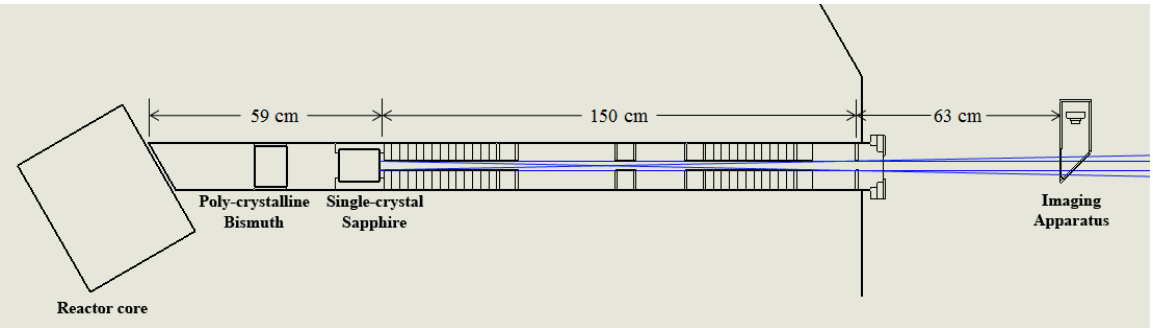


Figure 9: Schematic showing the approximate location of the imaging apparatus with respect to the reactor core (adapted from [21]).

## 3.4. Canon™ Digital Camera

The key element of the neutron imaging apparatus is the off-the-shelf Canon™ SD1100 IS digital camera. The camera was covered with black electric tape and placed in an electric tape-covered-Styrofoam stand. A black tape was used to prevent light reflection from the camera back to the mirror. Canon™ SD1100 IS was selected for this experiment in part due to the wide availability of open source software capable of enriching the camera's functionality. More specifically, the camera was modified to allow controlling the shutter time, subject distance (SD) and image sensor's sensitivity to light (ISO). The ability to modify the shutter time was perhaps most crucial as it enabled the user to control the time of light exposure. The open source software and a detailed user's guide is provided in [22].

## 3.5. Radiation Effects on CCD Cameras

Ionizing radiation is of a particular interest when discussing CCD cameras due to their silicon-based digital image sensors. The interaction between ionizing radiation and the silicon material typically manifests itself in the form of salt-and-pepper noise. An observer might recognize this type of noise as 'white spots' present in a digital image. In addition, the energy transferred from fast neutron scattering to the silicon material may result in displacements of silicon atoms from their crystalline lattice and consequently lead to a permanent damage of the camera. Furthermore, thermal neutrons, through the $^{28}Si(n,p)^{28}Al$ interaction, cause a proton-induced damage resulting in charge traps.

If placed in the beam's path, the camera is directly exposed to the radiation (neutrons, gammas, delays gammas, etc.) and is at risk of radiation damage. To correct for this, the camera is positioned outside of the beam's path and a mirror is used to reflect the light emitted from the conversion screen to the camera. However, to absorb the unattenuated thermal neutrons present along with the light emitted from the conversion screen, a mirror consisting of a lithium-6 glass and coated with a thin film of aluminum on its surface was used in the experiment. The neutron images produced with lithium-6 doped mirror were compared against images produced with an off-the-shelf mirror and showed insignificant difference. Histograms of digital pixel values were created to provide a quantitative measure of the radiation effects on the camera. Figure 10 shows histograms of images produced with the imaging apparatus containing an off-the-shelf mirror and without it. In addition, a histogram of the imaging apparatus placed in a radiation-absent environment is also shown as a control sample. The histograms suggest an increase in the digital pixel value mean as the imaging apparatus was moved from a

radiation-absent environment to an incident neutron beam setting used in the experiment. It also appears that the presence of a mirror in the light-tight box provided negligible attenuation of radiation since histograms presented in Figure 10 show very similar distributions.

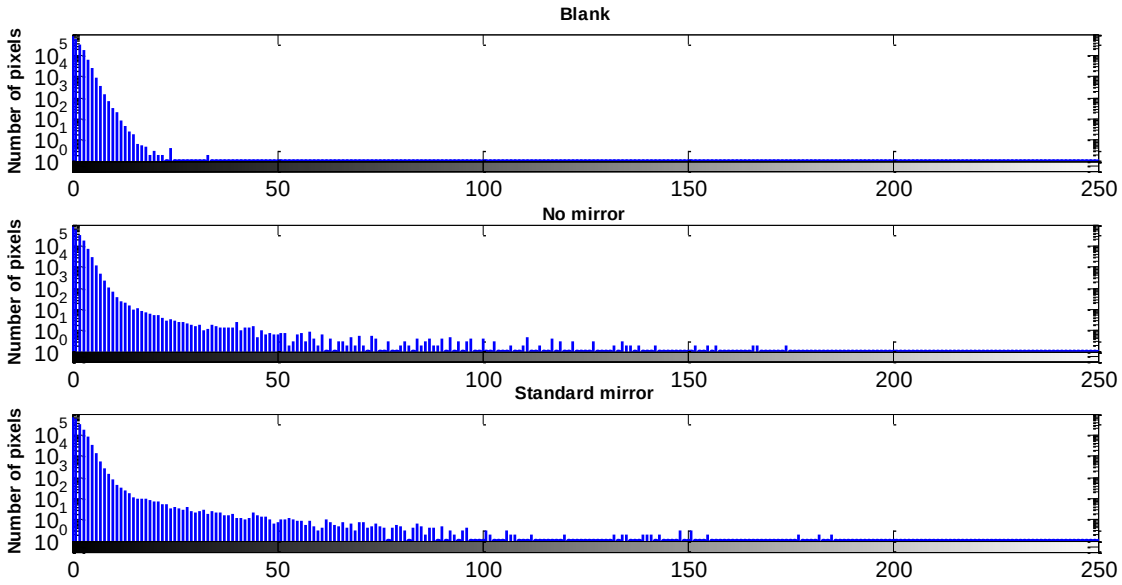


Figure 10: Histograms showing radiation effects on the camera (adapted from [21]).

## 3.6. Experimental Procedure

### 3.6.1. Camera Parameters

Although the digital camera used in the neutron imaging experiments had auto-focusing capability, the built-in algorithms select the optimal focus by comparing intensities of image pixels. Availability of light, image contrast, and subject distance (SD) are crucial elements required for this process. However, the light-tight box, in which

the camera was located during testing, clearly provided an unfavorable environment for this method.

The optimal focus was established manually using the added functionality of the open source software. An image of black-and-white checkerboard was created using MATLAB and printed on a glossy photograph paper. Several images of the checkerboard were captured with manually entered SD values. It was observed that non-optimal SD values contributed to distortions resulting in diverging checkerboard corners. Visual inspection led to selection of 190 mm as the optimal SD setting. For the sake of comparison,

Figure 11 shows pictures of the distorted checkerboard made with SD set to 150 mm and the optimal checkerboard image with SD set to 190 mm.

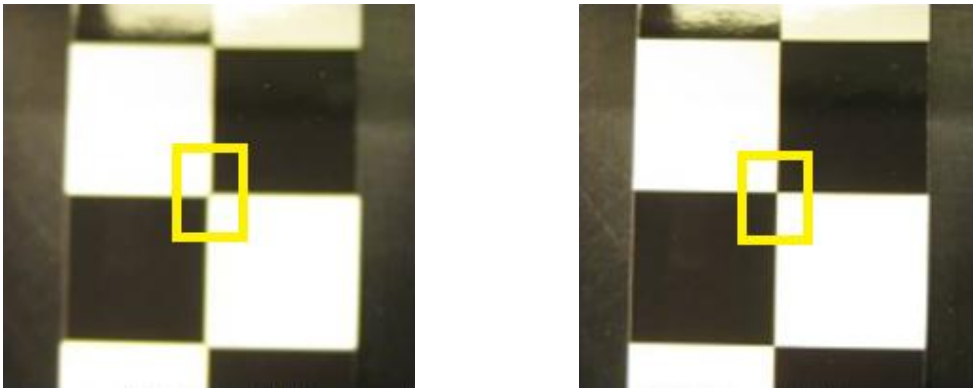

(a) (b)

Figure 11: Images of checkerboard taken with Canon™ SD1100 IS. The yellow rectangle outlines the camera's treatment of black rectangular corners with SD set to (a) 150 mm and (b) 190 mm (adapted from [21]).

In addition to the SD setting, several images of the neutron beam profile were taken to identify the optimal ISO setting. The ISO indicates the light sensitivity of the camera's sensor. Lower ISO values imply lower sensitivity of the camera to light and result in images with a fine grain. Such settings are often applied in well-lighted environments. However, in darker environments, capturing light is more difficult and often higher ISO values are applied. Nevertheless, higher ISO values result in noisier images [23]. Figure 12 shows images of the neutron beam profile captured with ISO 50 and ISO 200. The mean digital pixel value (DPV) in the beam umbra was 42 and 102 for ISO 50 and 200, respectively. Visual inspection again led to the selection of ISO 200 as the optimal light sensitivity.

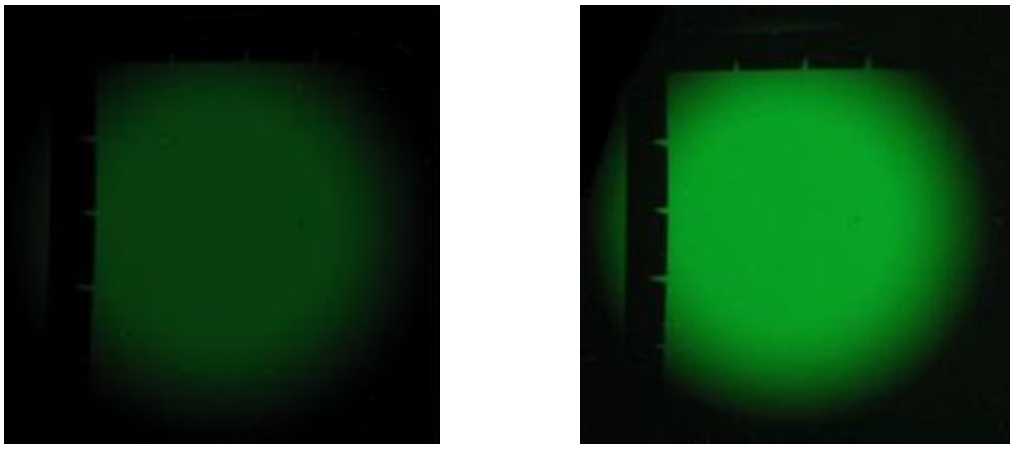

(a) (b)

Figure 12: Images of the neutron profile taken using Canon™ SD1100 IS with ISO set to (a) 50 and (b) 200 (adapted from [21]).

### 3.6.2. The Experiment

To complete system evaluation using MTF, NPS, and DQE experimental trials were conducted at the OSURR. The reactor power was raised to 250 kW, which provided a thermal equivalent neutron flux of $(4.75\pm0.11)\times10^{6}$ $cm^{-2}$ $s^{-1}$ at the sample location. Furthermore, to test the impact of fluence, measurements were taken during separate trials with exposure times of 8 s, 16 s, 32 s, 64 s, 80 s, and 101 s.

## 3.7. Data Processing

MTF calculations, as described in Chapter 2, require an edge image. Consequently, a strip of gadolinium foil (2.5 cm × 2.5 cm × 0.0127 cm) was vertically aligned on the exterior surface of the light-tight box. One edge of the strip was located approximately in the center of the neutron beam. Figure 3 shows an example of a gadolinium image taken during one of the trials. In addition, Figure 13 shows zoomed edge images of the gadolinium strip exposed to the neutron beam.

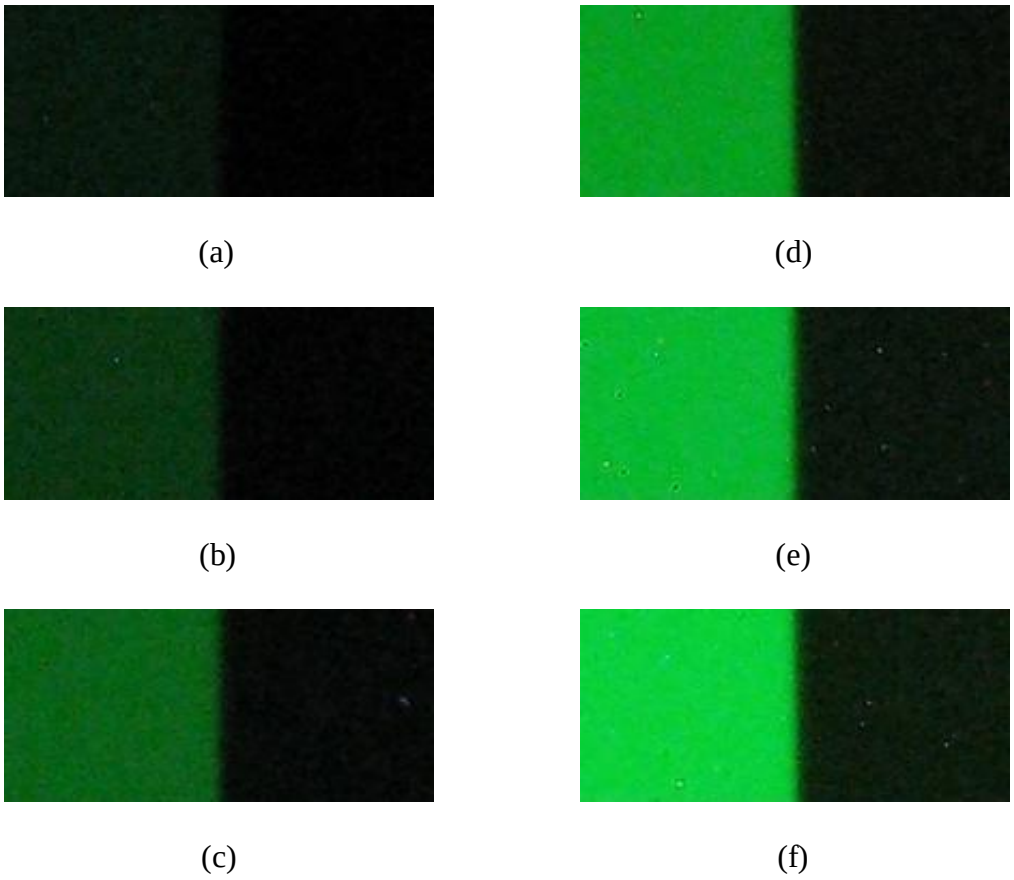


Figure 13: Enlarged view showing edge images of the gadolinium strip exposed for (a) 8, (b) 16, (c) 32, (d) 64, (e) 80, and (f) 101 seconds.

The process was then repeated without the gadolinium strip attached to the exterior of the box to capture neutron images necessary to characterize the background and provide data for NPS calculations. Zoomed-in views of these flat-field images are shown in Figure 14.

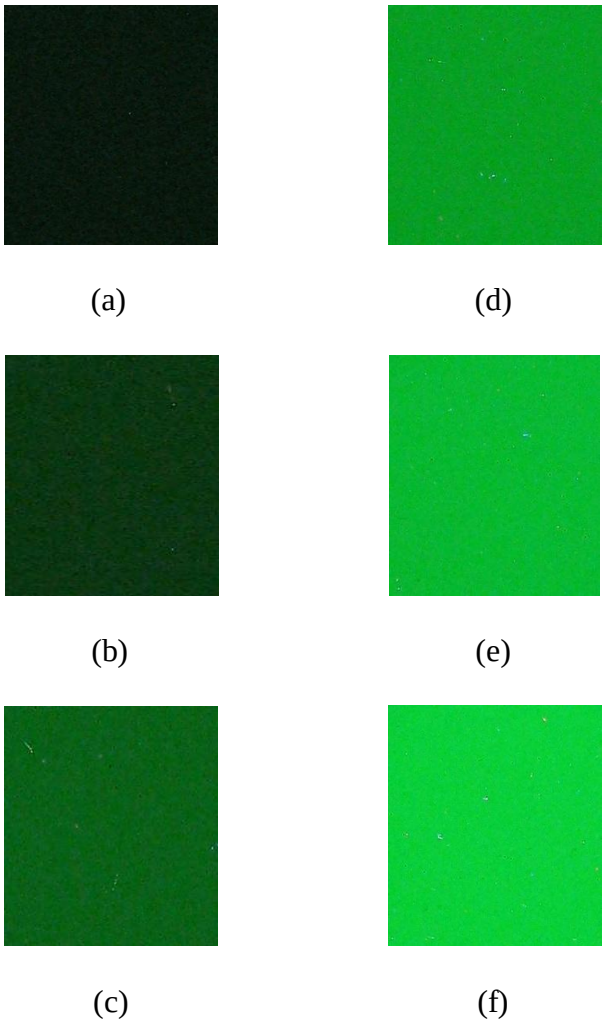


Figure 14: Enlarged view showing flat-field images developed using exposure time of (a) 8, (b) 16, (c) 32, (d) 64, (e) 80, and (f) 101 seconds.

The experimental data was acquired in the form of digital images (.jpeg format) and then analyzed with algorithms executed using MATLAB. MATLAB's Image Processing Toolbox was extensively used to convert images from RGB to grayscale and to process them with a Fast Fourier Transform (FFT).

# Chapter 4: Results and Discussion

## 4.1. MTF Analysis

### 4.1.1. ESF Graph

The images acquired with the gadolinium foil strip, shown in Figure 13, served as a basis for all MTF calculations. The images were first cropped to represent a rectangular region of 200(H) by 100(V) pixels. The edge boundary was approximately positioned in the vertical center of each image. To acquire a representative sample and eliminate the possible impact of vertical misalignment of the gadolinium strip on the light tight box, the one hundred horizontal rows were averaged to a single row. The single row converted to a grayscale, or the ESF, is shown in Figure 15. The y-axis, or the digital pixel value, ranges from 0 to 255, which corresponds to the grayscale range. A pixel value of 0 represents the weakest intensity (black), while a value of 255 represents the strongest intensity (255). In Figure 15, the curve labeled 'Checkerboard' represents the ESF of a checkerboard picture, shown in Figure 11 (b). The increased exposure time manifests in an increased step height. In other words, as the exposure time increased, the contrast between the background intensity and the edge intensity became more prominent. This corresponds to the differences visible with the naked eye in Figure 13.

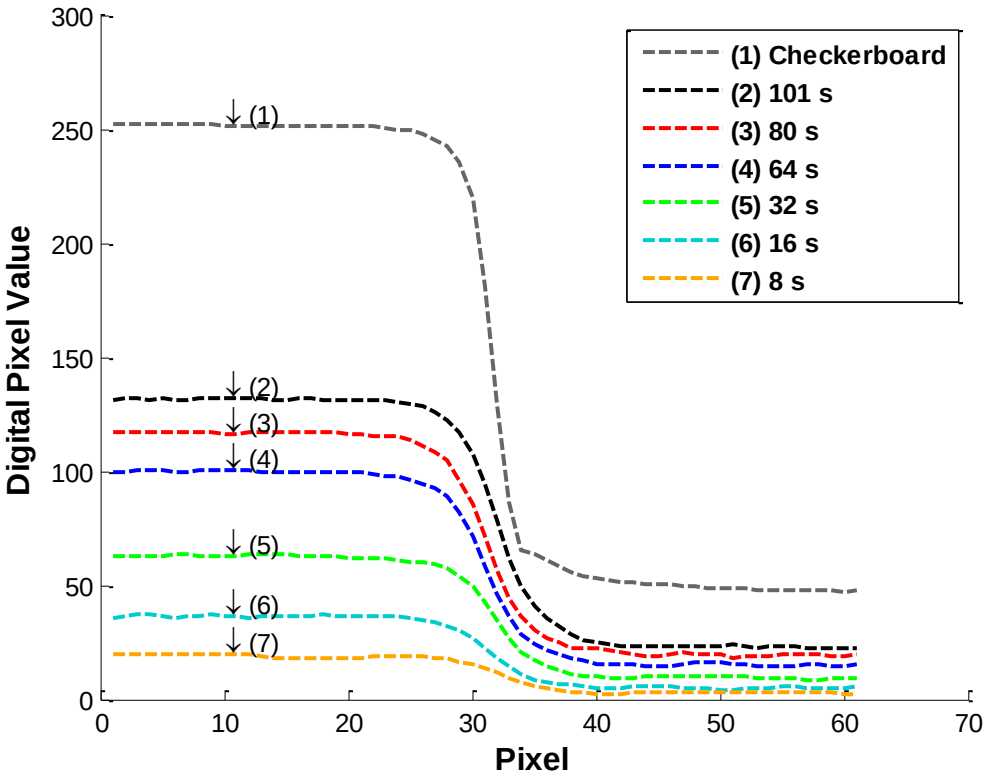


Figure 15: ESF of the checkerboard image and of the gadolinium foil strip exposed to the neutron beam for 8, 16, 32, 64, 80 and 101 seconds (adapted from [21]).

### 4.1.2. MTF Graph

Before frequency analysis, ESF curves were treated with a cubic spline and a Tukey window was applied to the differentiated ESF curves (LSF), which helped eliminate noise and preserve the shape of the data. MTF curves obtained by applying MATLAB's Fast Fourier Transform to the LSF curves are shown in Figure 16. The graph suggests that regardless of the chosen exposure time (fluence), MTF curves have approximately the same shape and decrease with increasing spatial frequency at the same rate. The difference among MTF curves due to the fluence appears rather

indistinguishable. The decrease in MTF agrees with the low-pass filter nature of a digital camera. Table 5, shown at the end of this chapter, provides information about Michelson's contrast and MTF10.

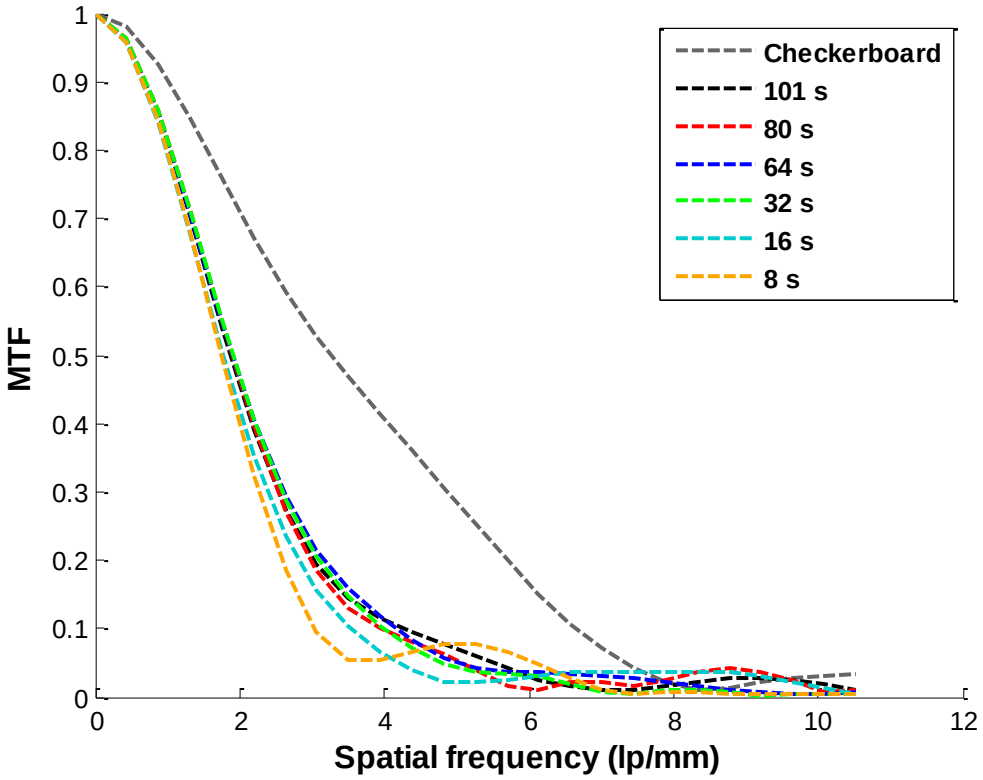


Figure 16: MTF curves of the gadolinium edge exposed to the neutron beam with exposure time as a parameter (adapted from [21]).

## 4.2. NPS Analysis

Flat-field images representing the neutron profile and shown in Figure 14 were used to calculate NPS curves. As described in Chapter 2, a procedure was adapted and

modified for the purpose of this study from the International Standard IEC 62220-1. More specifically, each flat-field image was divided into a series of regions of interest (ROI), where each ROI was a square of 64 by 64 pixels. The ROIs were formed according to the geometric arrangement shown in Figure 17 [14]. Starting in the upper left corner, each successive ROI was created by moving the previous 32 pixels horizontally to the right. When a boundary was reached, 32 pixels were moved down in the vertical direction and the process was repeated. This procedure generated a series of overlapping ROIs.

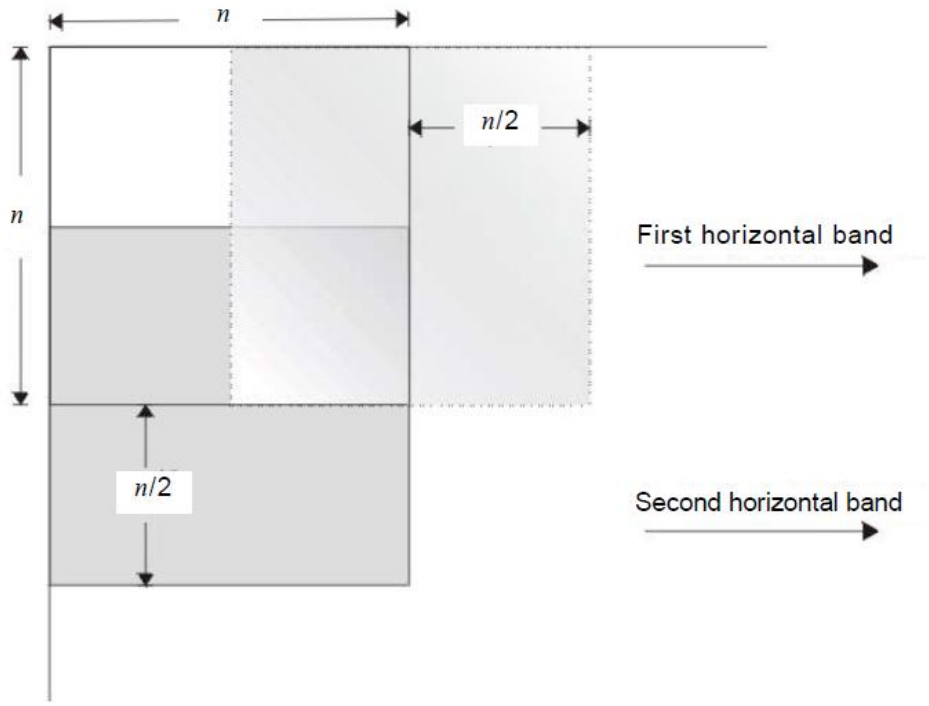


Figure 17: Method for generating ROIs (adapted from [14]). *n* represents the width/height of each ROI. A value of 64 pixels was used in this study.

Each ROI was treated with a two-dimensional, second-order polynomial to remove any trends caused by non-uniformities of the neutron detector [10]. In the next step, a two-dimensional Fourier transform was applied to every ROI. The results were averaged to describe a single, representative ROI. However, MATALB's two-dimensional Fourier transform method 'fft2' produces a two-dimensional NPS. To comply with the IEC 62202-1 standard, a Cartesian coordinate system was placed in the center of the average ROI. Sixteen rows above and below the spatial frequency axis (a total of 32 rows) were taken and averaged to form a one-dimensional representation of NPS.

The process described above and the theoretical background presented in Chapter 2 led to the development of the results shown in Figure 18. The graph clearly indicates the impact of exposure time (fluence) on the amount of noise experienced by the system. It shows that for shorter exposure times (i.e. 8 and 16 seconds), NPS is well-correlated and decreases with increasing spatial frequency. This relationship is not nearly as strong for longer exposure times (i.e. 80 and 101 seconds). In comparison, the neutrons entering the imaging device are assumed to be spatially independent and governed by Poisson statistics as described in Chapter 2. In Figure 4, a theoretical case described in Chapter 2, NPS appears to be constant and independent of the spatial frequency spectrum. The deviation of experimental NPS curves, shown in Figure 18, from this theoretical case suggests that the internal mechanisms of the digital device (gain and conversion process during image formation) introduce spatially correlated noise to the output that outweighs the Poisson distribution noise. However, as already mentioned this deviation is not uniform. The NPS curves of images taken with longer exposure times are smaller in

magnitude, more constant-shaped and seem to approach the theoretical case. This trend can be also seen in Table 5, which provides a numerical integral of the NPS curves. Therefore, fluence can be viewed as the system's filtering agent for noise of non-Poisson origin.

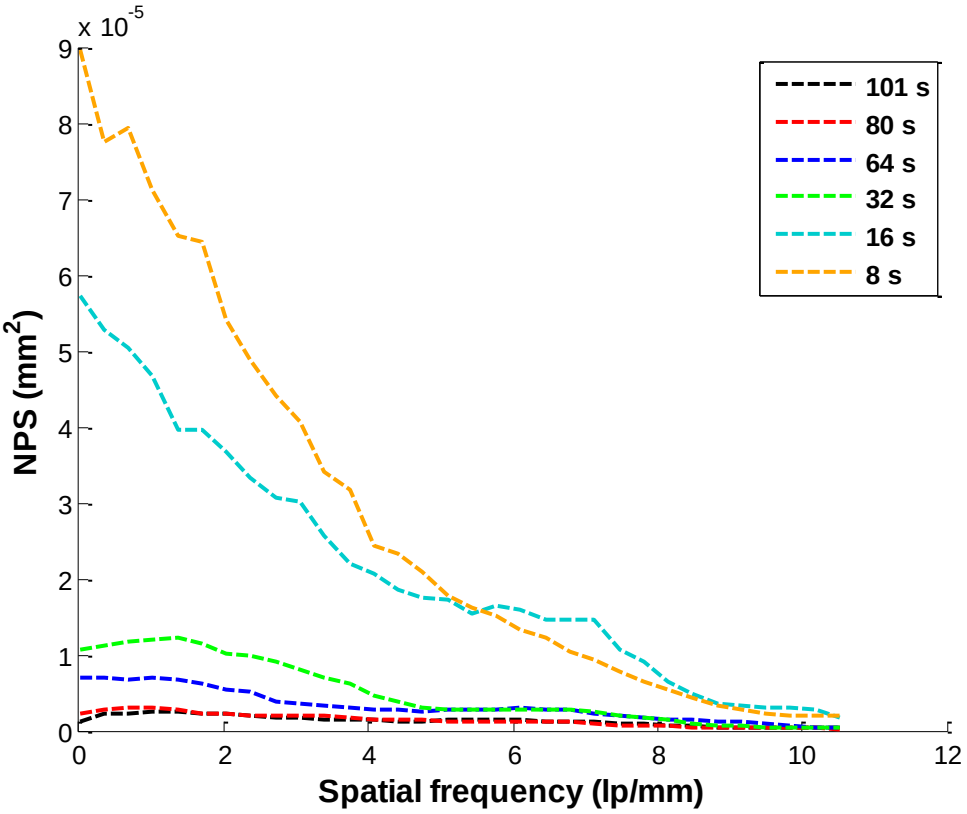


Figure 18: NPS curves of the flat-field images with exposure time as a parameter (adapted from [21]).

## 4.3. DQE Analysis

### 4.3.1. DQE Graph

As presented in Chapter 2, DQE combines the contributions from contrast and noise present in the system to describe its imaging and detail detection abilities. Results shown in Figure 16 and Figure 18 together with the information about the neutron source, presented in Table 3, were used to develop DQE curves graphed in Figure 19. The graph shows that for all exposure times DQE decreases with increasing spatial frequency. However, near lower spatial frequencies, the increased exposure time (fluence) contributes to a higher magnitude of DQE, which in turn translates to better detectability of details. The DQE values at lower spatial frequencies for exposure times of 64, 80, and 101 seconds are visibly higher than those for exposure time of 8, 16, or 32 seconds. This trend is also summarized in Table 5. Nevertheless, it is necessary to mention that beyond about 4 lp/mm, the DQE curves for all exposure times are nearly indistinguishable and approach a value of 0. This might be a consequence of the resolution limit reached by imaging system. A similar feature can be observed in Figure 16, where the MTF curves also appear grouped with little variation between each other beyond 4 lp/mm.

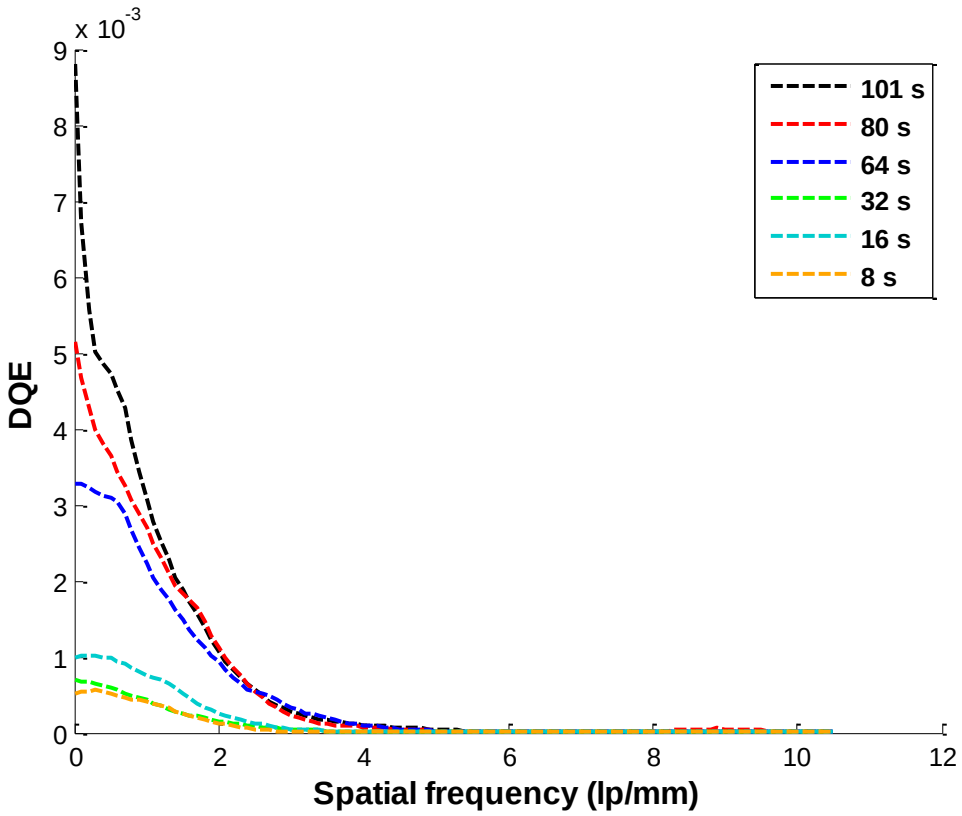


Figure 19: DQE curves characterizing image quality of the in-house developed neutron imaging device with exposure time as a parameter (adapted from [21]).

4.3.2. Comparison with MTF

Because of the similarities observed in graphed MTF and DQE results, it is necessary to examine these two metrics more closely. MTF and DQE curves were graphed on the same graph for each exposure time. However, because of similar trends observed at each exposure, Figure 20 shows the comparison between MTF and DQE produced using a 101-second exposure only. Graphs showing comparisons between MTF and DQE using other exposure times are shown in the appendix.

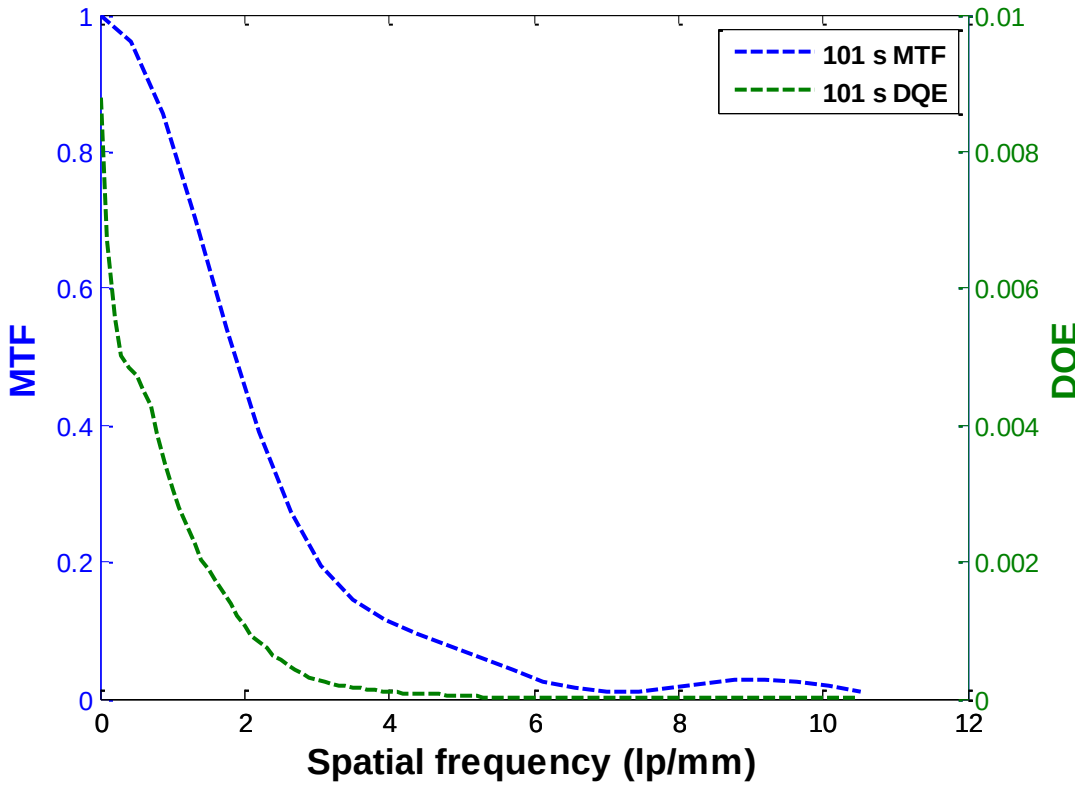


Figure 20: Graph showing similarities in the MTF and DQE curves of an imaging system operating at a 101-second exposure time.

Figure 20 aids in visualizing and comparing the shapes of MTF and DQE curves. Both curves decrease with increasing spatial frequency and share a very similar curvature. Such observation arises from the mathematical definition of DQE shown in (9). To reiterate, DQE is directly proportional to the square of MTF and inversely proportional to NPS. The other variables in the DQE equation refer to the number of incident neutrons and the recorded pixel intensity. These, however, are fixed constants

used in DQE calculations and serve as scaling factors. They do not vary DQE with respect to the spatial frequency spectrum. Furthermore, at high fluence levels, NPS is expected to be relatively independent of spatial frequency as mentioned earlier in the discussion in Section 4.2. With nearly all variables constant, it then becomes clear that the variations in DQE, at long exposure times, become almost solely dependent on the shape of the corresponding MTF curve. MTF curves of the experimental data, shown in Figure 16, range from 100% at a spatial frequency of 0 lp/mm and eventually approach 0% at higher spatial frequencies. Thus, it is clear why DQE, which accounts for the square of MTF, decreases to value of 0 more rapidly than MTF.

Table 5: Summary of quality metrics with exposure time as the experimental parameter (adapted from [21]).

| Exposure time (s) | 8 | 16 | 32 | 64 | 80 | 101 |
|---|---|---|---|---|---|---|
| Neutron fluence ($\times 10^6$ $cm^{-2}$) | 38 ± 0.76 | 76 ± 1.5 | 152 ± 3.0 | 304 ± 6.1 | 380 ± 7.6 | 480 ± 9.6 |
| Michelson Contrast | 0.75 ± 0.08 | 0.76 ± 0.08 | 0.75 ± 0.08 | 0.74 ± 0.07 | 0.72 ± 0.07 | 0.71 ± 0.07 |
| 10% MTF | 3.0 | 4.6 | 5.3 | 5.5 | 5.3 | 5.8 |
| Total NPS ($\times 10^{-5}$ $mm^2$) | 29.0 | 22.0 | 5.2 | 3.4 | 1.5 | 1.4 |
| Total DQE (%) | 0.080 | 0.17 | 0.10 | 0.53 | 0.64 | 0.77 |

# Chapter 5: Conclusion

The study described in this thesis had three main objectives related to characterization of a low-cost digital neutron imaging device. An in-house developed neutron imaging device was prepared with an off-the-shelf digital camera as its key component. A series of trials aimed at capturing images of a neutron profile and a gadolinium foil target was performed at the OSU Research Reactor. During the trials, fluence, or the amount of neutrons incident onto an area, was varied by controlling the exposure time. This experimental parameter was changed to examine the importance of fluence on the quality of images and the associated noise level. The collected data, in form of digital images, were analyzed with the assistance of MATLAB. The analysis consisted of applying the modulation transfer function, the noise power spectrum, and the detective quantum efficiency to quantify the system's contrast and detail detectability.

## 5.1. Contributions

The experimental results served as a foundation for analysis and discussion directed towards informing the neutron radiography community of the issues associated with noise present in neutron radiography systems and the inefficiency of using the modulation transfer function as the only metric to quantify image quality. The outcomes of the experiments, methods used, and an in-depth discussion were published in the Nuclear Instruments and Methods in Physics Research Section A, listed in the References

as [10]. The breath and complexity of material led to another journal paper that was submitted to IEEE TNS for a review in February of 2012 and is listed in References as [21].

## 5.2. Future Work

The analysis performed as a part of this study gave rise to a number of ideas and possible future investigations in the area of neutron radiography using the tools developed by the Nuclear Analysis and Radiation Sensor Laboratory at The Ohio State University.

During a series of trials, a Canon™ SD1100 IS (IXUS 80) camera, modified with open source software, was used for remote triggering and selection of parameters including the exposure time, ISO, and SD values. However, the open source software offered only manual selection of parameters. It is worthwhile to consider a development of a GUI-based, interactive MATLAB program that would allow remote control of all parameters from a stationary computer connected to the imaging camera. This would increase safe handling of the device and allow for real-time analysis of MTF, NPS, and DQE results. Furthermore, eliminating the need to remove the camera form the light-tight box and manually set software parameters would dismiss a potential source of errors related to proper positioning of the camera during successive trials.

Closely related is the choice of Canon™ SD1100 IS (IXUS 80) as the imaging device. A selection of different digital cameras might provide additional insight into the neutron radiography apparatus. It would be interesting to test a camera from a different

manufacturer with technical properties similar to that of Canon's SD1100 IS and compare the experimental results between the two. Perhaps such study would help describe the input-to-output conversion mechanisms present in digital cameras and see which one contributes higher levels of noise.

Another key component used in the neutron imaging apparatus was the $^{6}$LiF(ZnS) scintillation screen used to convert neutrons to particles of light. It is most likely that this screen acted as the quantum sink, a region marred by inefficiencies and loss of information. A new experiment that tests different scintillation screens might shed light on their associated efficiencies and aid in determining their impact on MTF, NPS, and DQE.

One of the main observations resulting from this study is the impact of fluence on the quality of produced images and the noise present in them. However, it appears that beyond a certain limit, the exposure time (fluence) plays a very small role in the said characteristics. This points the discussion to examining the reasons behind this limit and the possibility of overcoming it. In most testing scenarios, a shorter irradiation time is preferred. It would be thus helpful to identify the most optimal exposure time and the tradeoffs between quality of images and noise.

## 5.3. Summary

The successful application of MTF, NPS, and DQE to a neutron radiography system has validated the initial hypothesis that MTF alone is not a sufficient technique in quantifying the quality of images produced by such systems. It was found that MTF is a

useful tool in determining the system's spatial resolution and contrast. The shape and magnitude of NPS curves can be used to measure the presence and strength of noise. Systems exposed to high fluence levels tend to result in NPS curves that are fairly constant across the spatial frequency spectrum. Furthermore, the experimental results have shown that DQE, which combines the effects of MTF and NPS, is highly influenced by MTF at higher fluence levels. The detectability of small details can be thus mainly attributed to MTF in cases with high fluence or exposure time.

References


1. Knoll, G.F., *Radiation detection and measurement*. 4th ed2010, Hoboken, N.J.: John Wiley. xxvi, 830 p.
2. Heller, A.K., Brenizer, J.S., *Neutron Radiography*, in *Neutron imaging and its applications*. p. 67.
3. Satija, R., et al., *In situ neutron imaging technique for evaluation of water management systems in operating PEM fuel cells.* Journal of Power Sources, 2004. **129**(2): p. 238-245.
4. Ferreira, F.J.O., V.R. Crispim, and A.X. Silva, *Detection of drugs and explosives using neutron computerized tomography and artificial intelligence techniques.* Applied Radiation and Isotopes, 2010. **68**(6): p. 1012-1017.
5. Ryan, J.M., et al. *Development and performance of the Fast Neutron Imaging Telescope for SNM detection*. 2008. Orlando, FL, USA: SPIE.
6. Marleau, P., et al., *Advances in imaging fission neutrons with a neutron scatter camera*, in *2007 Ieee Nuclear Science Symposium Conference Record, Vols 1-11*2007, Ieee: New York. p. 170-172.
7. Center, M.N.R. [cited 2012 30 April 2012]; Available from: http://mnrc.ucdavis.edu/radiography.html.
8. Bandyopadhyay, P. *Periodic Table*. [cited 2012 16 May]; Available from: http://www.csrri.iit.edu/periodic-table.html.
9. Baum, E.M. and S.D. Travis, *Nuclides and isotopes : chart of the nuclides*. 17th ed2010, Schenectady, NY: Bechtel : Knolls Atomic Power Laboratory. vi, 92 p.
10. Lewandowski, R., L. Cao, and D. Turkoglu, *Noise evaluation of a digital neutron imaging device.* Nuclear Instruments and Methods in Physics Research Section A: Accelerators, Spectrometers, Detectors and Associated Equipment, 2012. **674**(0): p. 46-50.
11. Koren, N. *Understanding image sharpness and MTF* [cited 2012 April 30]; Available from: http://www.normankoren.com/Tutorials/MTF.html.
12. Michelson, A.A., *Studies in optics*. The University of Chicago science series1927, Chicago, Ill.,: The University of Chicago Press. ix, 176 p.
13. Perry, B., *Algorithm for MTF Estimation by Histogram Modeling of an Edge*, in *Center for Imaging Science*2000, Rochester Institute of Technology: Rochester, NY.
14. IEC, *IEC 62220-1 2003 Medical Electrical Equipment-Characteristics of Digital X-ray Imaging Devices-Part 1: Determination of the Detective Quantum Efficiency* 2003, Newark,NY.
15. Figliola, R.S. and D.E. Beasley, *Theory and design for mechanical measurements*. 5th ed2011, Hoboken, NJ: John Wiley. ix, 590 p.

16. Workman, A. and D.S. Brettle, *Physical performance measures of radiographic imaging systems.* Dentomaxillofacial Radiology, 1997. **26**(3): p. 139-146.
17. Shaw, R., *EVALUATING EFFICIENCY OF IMAGING PROCESSES.* Reports on Progress in Physics, 1978. **41**(7): p. 1103-1155.
18. Tapiovaara, M.J. and R.F. Wagner, *SNR AND NOISE MEASUREMENTS FOR MEDICAL IMAGING - IA PRACTICAL APPROACH BASED ON STATISTICAL DECISION-THEORY.* Physics in Medicine and Biology, 1993. **38**(1): p. 71-92.
19. T.Dobbins, J., *Handbook of medical imaging vol 1. physics and psychophysics*, ed. H.L.K. Jacob Beutel, Richard L.Van Metter. Vol. 1. 2000, Bellingham: SPIE press. 949.
20. Turkoglu, D., et al., *Characterization of a new external neutron beam facility at the Ohio State University.* Journal of Radioanalytical and Nuclear Chemistry, 2012. **291**(2): p. 321-327.
21. Turkoglu, D., Lewandowski, Radoslaw, Cao, Lei, *A Low-cost Neutron Radiography Device and the Discussion of MTF and DQE*. IEEE Transactions on Nuclear Science, 2012. **IN REVIEW**.
22. *Canon Hack Development Kit*. [cited 2012 16 May]; Available from: http://chdk.wikia.com/wiki/CHDK.
23. Rowse, D. *ISO Settings in Digital Photography*. [cited 2012 30 April]; Available from: http://digital-photography-school.com/iso-settings.

Appendix A: Comparison of MTF and DQE Graphs

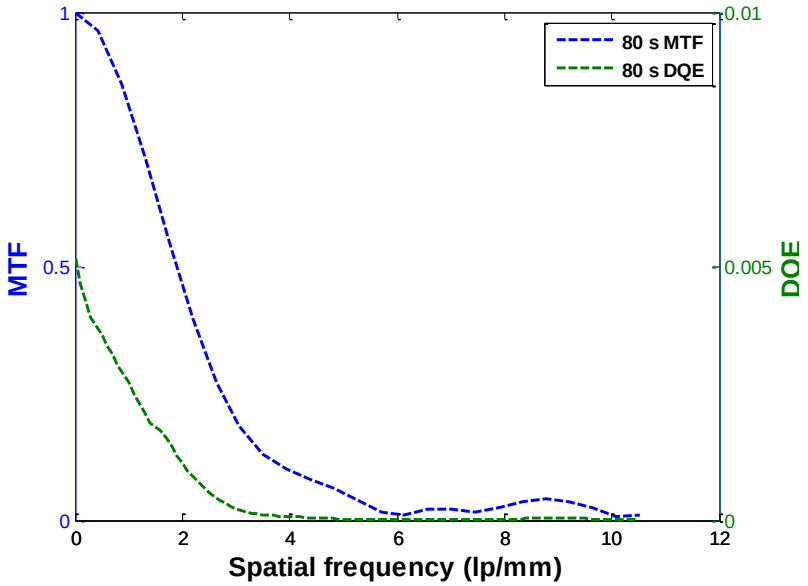


Figure 21: Graph showing similarities in the MTF and DQE curves of an imaging system operating at a 80-second exposure time.

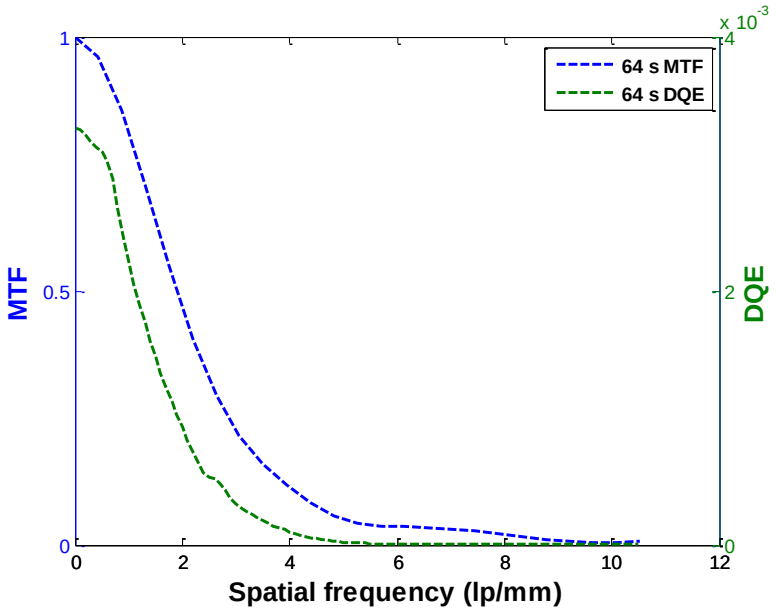


Figure 22: Graph showing similarities in the MTF and DQE curves of an imaging system operating at a 64-second exposure time

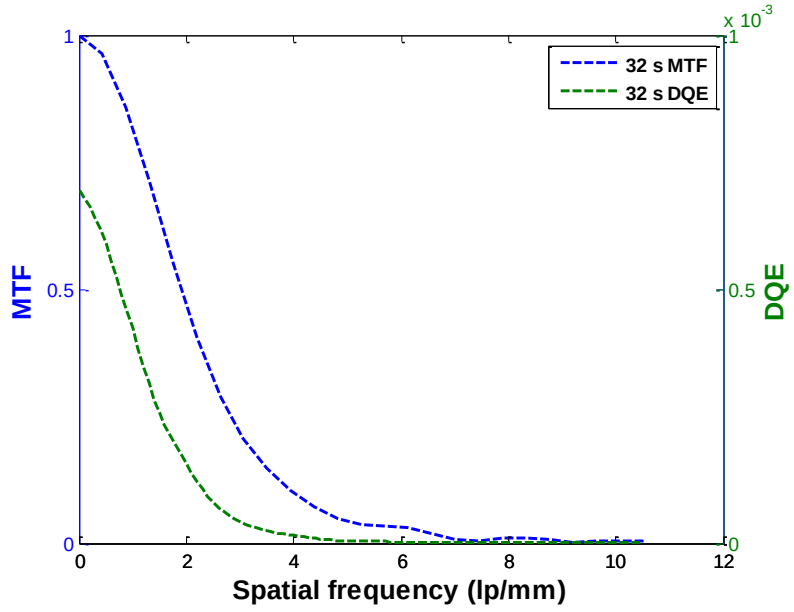


Figure 23: Graph showing similarities in the MTF and DQE curves of an imaging system operating at a 32-second exposure time.

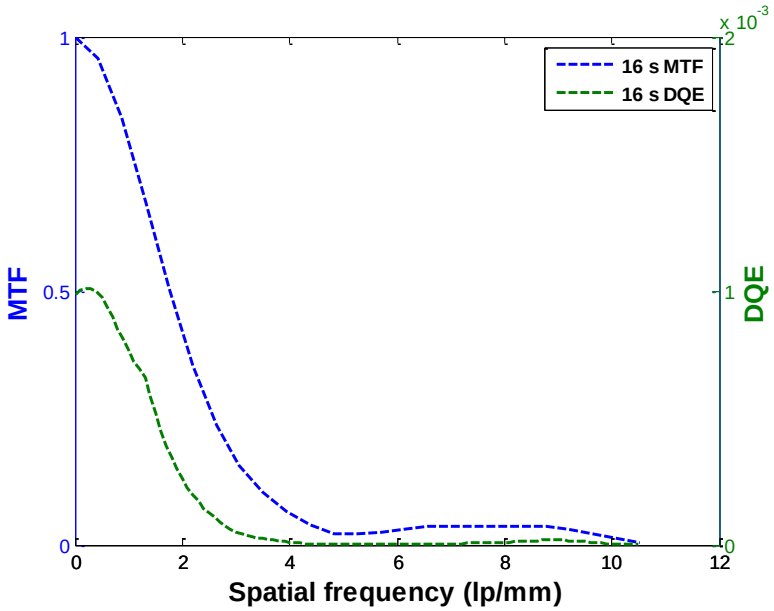


Figure 24: Graph showing similarities in the MTF and DQE curves of an imaging system operating at a 16-second exposure time.

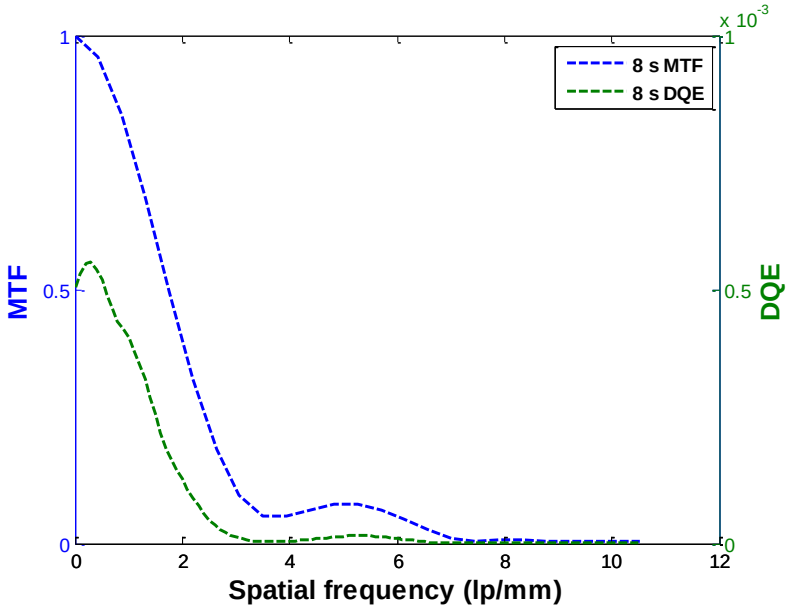


Figure 25: Graph showing similarities in the MTF and DQE curves of an imaging system operating at a 8-second exposure time.

# Appendix B: MATLAB Code

Work of Danyal Turkoglu and Radoslaw Lewandowski

```
%Last updated: 2/11/2012

function DQE_Gd3(color, check)
% Get to correct directory
% cd \Users\Danyal\dropbox\IEEE_data\Matlab_WS
% cd \Users\Rod\dropbox\IEEE_data\Matlab_WS
%%%%%%% Inputs
%       color = 'Gray', Use Grayscale image
%               'Green', Use green component
%       check = 1, plot ESF and LSF to check smoothing and filtering
%                  process
%               0  no check (default)
%%
close all

% clear all, DQE_Gd3('Gray',0)
if nargin == 0
    color = 'Gray';
    check = 0;
elseif nargin == 1
    check = 0;
end
%% Images to be used
imageRecord = {'checkerboard.jpg'; %    'gd_lightsource2.jpg'
    'gd_101sec.jpg'
    'gd_80sec.jpg'
    'gd_64s_190sd.jpg'
    'gd_32sec.jpg'
    'gd_16sec.jpg'
    'gd_8sec.jpg'
    'gdb101s_background2.jpg'
    'gd_b80s_background2.jpg'
    'gd_b64s_background2.jpg'
    'gd_b32s_background2.jpg'
    'gd_b16s_background2.jpg'
    'gd_b8s_background2.jpg'};
%% Read images
for i = 1:size(imageRecord,1)
    imageName = char(imageRecord(i));
```

```
    image = imread(imageName);
    storeName = imageName(1:6);
    nameRecord(i) = {storeName};
    imagesRGB.(storeName) = image;
    if color == 'Gray'
        images.(storeName) = rgb2gray(image);
    elseif color == 'Green'
        images.(storeName) = image(:,:,2);
    end
end
clear image
%% Parameters
camera_parameters;
plot_parameters;
%% Create Edge Spread Function (ESF) and Line Spread Function (LSF)
for i = 1:7
    name = char(nameRecord(i));
    image = images.(name);
    x1 = 70; x2 = 130; % bounds
    ESF_raw.(name) = sum(image)/size(image,1);
    ESF_raw.(name)= ESF_raw.(name)(1,x1:x2);
    x = [1:(x2-x1+1)];
    [sp,values] = spaps(x ,ESF_raw.(name),1); % cubic-spline
    ESF_sp.(name) = values;
    %     if check == 1
    %         figure(1)
    %         plot(ESF_raw.(name),'k')
    %         hold on
    %         plot(ESF_sp.(name),'r'), shg
    %         pause
    %         hold off
    %     end
    LSF_raw.(name) = -diff(ESF_raw.(name));
    LSF.(name) = -diff(ESF_sp.(name));
    filter_window = [zeros(1,20),tukeywin(size(x,2)-
40,.6)',zeros(1,20)];
    LSF_filtered.(name) = filter_window(1:(x2-x1)).*LSF.(name);
    %     if i == 7
    %         x = [1:(x2-x1)];
    %         [LSF_max.(name), LSF_xmax.(name)] =
max(LSF_filtered.(name));
    %         y = 1;
    %         [sp,LSF_filtered_sp_l.(name)] =
spaps(x(1:LSF_xmax.(name)-y) ,LSF_filtered.(name)(1:LSF_xmax.(name)-
y),1); % cubic-spline
    %         [sp,LSF_filtered_sp_r.(name)] =
spaps(x(LSF_xmax.(name)+y:end)
,LSF_filtered.(name)(LSF_xmax.(name)+y:end),1); % cubic-spline
    %         LSF_final.(name) =
[LSF_filtered_sp_l.(name),LSF_filtered.(name)(LSF_xmax.(name)-
y+1:LSF_xmax.(name)+y-1),LSF_filtered_sp_r.(name)];
    %     else
```

```
    LSF_final.(name) = LSF_filtered.(name);
    if i == 7
        LSF_final.(name)(22:24)=[0,0,0];
    end
    %     end
    if check == 1
        if i == 7
            figure(2)
            plot(filter_window*max(LSF.(name)),'y')
            hold on
            plot(LSF_raw.(name), 'b')
            plot(LSF.(name), 'r')
            plot(LSF_filtered.(name), 'k'), shg
            plot(LSF_final.(name), 'g'), shg
            legend('Tukey window (scaled)','Untreated ESF','ESF with
cubic spline fit','Filtered LSF','Final LSF')
            pause
            hold off
        end
    end
    %% Plot ESF
    figure(3)
    hold on

plot(ESF_sp.(name),styles(i,1:2),'Color',[str2num(char(MTF_colors(i)))]
,'LineWidth',width)
    text(10,ESF_sp.(name)(10)+6,['\downarrow (',num2str(i),')'],...
        'HorizontalAlignment','left')
    %     shg,pause
    figure(7),hold on
    subplot(2,2,1)

plot(ESF_sp.(name),styles(i,1:2),'Color',[str2num(char(MTF_colors(i)))]
,'LineWidth',width)
    text(10,ESF_sp.(name)(10)+6,['\downarrow (',num2str(i),')'],...
        'HorizontalAlignment','left')



    %% Calculate Modulation Transfer Function
    %     if i == 7
    %         LSF_final.(name) = LSF_filtered.(name)
    %     end
    MTF.(name) = fftshift(abs(fft(LSF_final.(name))));
    [MTF_max.(name), MTF_xmax.(name)] = max(MTF.(name));
    MTF.(name)=MTF.(name)/MTF_max.(name); % normalize
    figure(4)
    hold on
    plot(spatial_frequency,
MTF.(name)(MTF_xmax.(name):(MTF_xmax.(name)+p-1))...

,styles(i,1:2),'Color',[str2num(char(MTF_colors(i)))],'LineWidth',width
)
    %     text(2,MTF.(name)(2+i),['\leftarrow (',num2str(i),')'],...
```

```
    %         'HorizontalAlignment','left')
    %
    figure(7), hold on
    subplot(2,2,2)
    xmin = (MTF_xmax.(name));
    xmax = (MTF_xmax.(name)+p-1);
    plot(spatial_frequency, MTF.(name)(xmin:xmax)...

,styles(i,1:2),'Color',[str2num(char(MTF_colors(i)))],'LineWidth',width
)

    %     spatial_frequency_spline, spatial_frequency, whos, pause
    x = spatial_frequency(3:end-1);
    y= MTF.(name)(xmin+3:xmax);
    xx = spatial_frequency_spline;
    yy = spline(x,y,xx);
    %     figure(12)
    %     whos
    %     plot(xx,yy), pause
    MTF_f = find(floor(100*yy)==10);
    MTF_c = find(ceil(100*yy)==10);
    MTF10.(name) = spatial_frequency_spline(max(MTF_f))+
spatial_frequency_spline(min(MTF_c))/2;

end
%% Noise Power Spectrum
%NPS_parameters -> This call needs to be inside of the for loop. RL.
for ii=8:13
    NPS_parameters
    name = char(nameRecord(ii));
    if check == 2
        figure(20)
        %     I = rgb2gray(imread('gdb101s_background.jpg'));
        [xx,yy]=size(images.(name));
        [XX,YY] = meshgrid(1:yy,1:xx);
        mesh(XX,YY,log(double(images.(name))));
        shading interp
        colorbar
        shg,pause
    end
    [x_max y_max] = size(images.(name));
    if rem(x_max,shift)~= 0
        x_max = floor(x_max/shift)*shift;
    end
    if rem(y_max,shift)~= 0
        y_max = floor(y_max/shift)*shift;
    end

    %Create an 'average' background image
    %Adapted from IEC62220-1
    for i = y_min: shift: y_max
        for j = x_min: shift: x_max
            %Crop image, remove trend and find local NPS
```

```
            localNoise = double(imcrop(images.(name), [x_min, y_min,
roiSize-1, roiSize-1]));
            localNoise = localNoise/max(max(localNoise)); %I added
'max' normalization here. RL
            fit = mm2dpfit(X,Y, localNoise, 2,2);
            trend = mm2dpval(fit,X,Y);
            localNoiseCorrected = localNoise-trend;
            %localNoiseCorrected = localNoiseCorrected.*Ham;
            localNPS = (abs(fftshift(fft2(localNoiseCorrected))).^2);

            %Update variables
            sumNoise = sumNoise + localNoise;
            sumNPS = sumNPS + localNPS;
            no_of_ROI = no_of_ROI + 1;
        end
    end

    %Averaging process
    %noiseImageAvg is a 64 x 64 pixels image
    noiseImageAvg = sumNoise./no_of_ROI;
    %Mean pixel value of image
    meanPixel.(name) = mean(mean(noiseImageAvg));

    %2-dimensional NPS
    NPS2D =
sumNPS*effective_pixel_size*effective_pixel_size/(roiSize*roiSize*no_of
_ROI);

    %Conversion from 2D to 1D NPS
    NPS = zeros(1,32);
    x_origin = 33;
    y_origin = 33;
    j = 0;
    for i = -7:1:7
        if i == 0
            continue
        end
        NPStemp = NPS2D(x_origin+i, y_origin:64);
        NPS = NPS + NPStemp;
        j = j+1;
    end
    NPS = NPS./j;
    NPSf.(name) = smooth(NPS',5)';
    %% Define plotting region
    p2 = 32; % number of pixels to plot
    spatial_frequency2 = pixels_per_mm*0.5 * [0:p2-1]/(p2-1)';
    figure(5), hold on
    plot(spatial_frequency2, NPSf.(name),styles(ii-
6,1:2),'Color',[str2num(char(MTF_colors(ii-6)))],'LineWidth',width)
    figure(7)
    subplot(2,2,3)
    plot(spatial_frequency2, NPSf.(name),styles(ii-
6,1:2),'Color',[str2num(char(MTF_colors(ii-6)))],'LineWidth',width)
```

```
    hold on


end

%% Detective Quantum Efficiency
DQE_parameters;
for ii = 2:7
    name = char(nameRecord(ii));
    name2 = char(nameRecord(ii+6)); % name for background results
    NPS = NPSf.(char(nameRecord(ii+6)));
    %Normalized NPS by the square of the mean pixel value
    NNPS.(name) = (interp1(spatial_frequency2, NPS, spatial_frequency3,
'pchip'))./(meanPixel.(name2).^2);
    % MTF Squared
    MTF_sq.(name) = (interp1(spatial_frequency,
MTF.(name)(MTF_xmax.(name):(MTF_xmax.(name)+p-1)),
spatial_frequency3, 'pchip')).^2;

    DQE.(name) = MTF_sq.(name)./(NNPS.(name) .*N.(name));
    DQE_log.(name) = log(DQE.(name));
    DQE_integral.(name) = trapz(spatial_frequency3, DQE.(name));

    NPSi.(name) = trapz(spatial_frequency2, NPSf.(name2));
    %% figure(6) DQE of at all exposure times
    figure (6), hold on
    semilogy(spatial_frequency3,
DQE.(name),styles(ii,1:2),'Color',[str2num(char(MTF_colors(ii)))],'Line
Width',width);
    figure(7)
    subplot(2,2,4)
    plot(spatial_frequency3,
DQE.(name),styles(ii,1:2),'Color',[str2num(char(MTF_colors(ii)))],'Line
Width',width);
    hold on
end



plot_labels
display_results
if check == 1
    DQE_MTF_comparison
end
save = input('Do you want to save figures? (y/n)    : ','s');
if save == 'y'
    %     figure(3)
    %     print -painters -dpdf -r600 ESFfig.pdf
    %     print -painters -dpdf -r600 ESFfig.eps
    %     figure(4)
    %     print -painters -dpdf -r600 MTFfig.pdf
    %     print -painters -dpdf -r600 MTFfig.eps
```

```
    %     figure(5)
    %     print -painters -dpdf -r600 NPSfig.pdf
    %     print -painters -dpdf -r600 NPSfig.eps
    %     figure(6)
    %     print -painters -dpdf -r600 DQEfig.pdf
    %     print -painters -dpdf -r600 DQEfig.eps
    figure(7)
    print -painters -dpdf -r600 fig6pdf.pdf
    print -painters -dpdf -r600 fig6eps.eps
end

    function DQE_MTF_comparison
        font = 14;
        width = 1.5;
        for i = 2:7
            % Comparison between MTF and DQEs
            name = char(nameRecord(i));
            figure(i+8)
            [AX,H1,H2] =
plotyy(spatial_frequency,MTF.(name)(MTF_xmax.(name):(MTF_xmax.(name)+p-
1)),spatial_frequency3,DQE.(name),'plot');
            set(get(AX(1),'Ylabel'),'String','\bfMTF','FontSize', font)
            set(get(AX(2),'Ylabel'),'String','\bfDQE','FontSize', font)
            xlabel('\bfSpatial frequency (lp/mm)', 'FontSize', font)
            set(H1, 'LineWidth', width, 'LineStyle', '--')
            set(H2, 'LineWidth', width, 'LineStyle','--')

%             set(H1, 'Color', [str2num(char(MTF_colors(2)))],
'LineWidth', width, 'LineStyle', '--')
%             set(H2, 'Color', [str2num(char(MTF_colors(2)))],
'LineWidth', width, 'LineStyle','--')
%            legend('\bf64 s MTF', '\bf64 s DQE')
        end
        figure(10)
        legend('\bf101 s MTF', '\bf101 s DQE')
        figure(11)
        legend('\bf80 s MTF', '\bf80 s DQE')
        figure(12)
        legend('\bf64 s MTF', '\bf64 s DQE')
        figure(13)
        legend('\bf32 s MTF', '\bf32 s DQE')
        figure(14)
        legend('\bf16 s MTF', '\bf16 s DQE')
        figure(15)
        legend('\bf8 s MTF', '\bf8 s DQE')

    end

    function camera_parameters
        %%
        image_size = 25; %mm, Gadolinium foil
        number_of_pixels = 526; % pixels
        effective_pixel_size = image_size / number_of_pixels;
```

```
        pixels_per_um = 526 / (25*10^3);
        pixels_per_mm = 526 / 25;
        lines_per_mm = 1/effective_pixel_size;
        lp_per_mm = lines_per_mm/2; % cut-off frequency
        disp(['The effective pixel size of image is ',
num2str(effective_pixel_size*10^3),' micrometers'])
        disp(['The cut-off frequency is ', num2str(lp_per_mm),' lines
pairs per mm'])
        %% Define plotting region
        p = 25; % number of pixels to plot
        spatial_frequency = pixels_per_mm*0.5 * [0:p-1]/(p-1)';
        spatial_frequency_spline = pixels_per_mm*0.5 * [0:0.25:p-1]/(p-
1)';
    end

    function plot_parameters
        width = 1.5;
        font = 14.0;
        MTF_colors={'.4 .4 .4';
            '0 0 0';
            '1 0 0';
            '0 0 1';
            '0 1 0';
            '0    0.8    0.8';
            ' 1.0     0.6471         0';
            '0.5804         0    0.8275';};
        styles = ['--';
            '--';
            '--';
            '--';
            '--';
            '--';];
    end

    function plot_labels
        width = 2.0;
        font = 12.0;
        figure(3)
        legend('\bf(1) Checkerboard','\bf(2) 101 s','\bf(3) 80
s','\bf(4) 64 s','\bf(5) 32 s','\bf(6) 16 s','\bf(7) 8 s')
        xlabel('\bfPixel', 'FontSize', font)
        ylabel('\bfDigital Pixel Value', 'FontSize', font)
        figure(4)
        legend('\bfCheckerboard','\bf101 s','\bf80 s','\bf64 s','\bf32
s','\bf16 s','\bf8 s')
        xlabel('\bfSpatial frequency (lp/mm)','FontSize', font)
        ylabel('\bfMTF', 'FontSize', font)
        figure(5)
        xlabel('\bfSpatial frequency (lp/mm)', 'FontSize', font)
        ylabel('\bfNPS (mm^2)', 'FontSize', font)
        legend('\bf101 s','\bf80 s','\bf64 s','\bf32 s','\bf16 s','\bf8
s')
```

```
        figure(6)
        legend('\bf101 s','\bf80 s','\bf64 s','\bf32 s','\bf16 s','\bf8
s')
        xlabel('\bfSpatial frequency (lp/mm)', 'FontSize', font)
        ylabel('\bfDQE', 'FontSize', font)
        figure(7)
        h = subplot(2,2,1);
        legend('\bf(1) Checkerboard','\bf(2) 101 s','\bf(3) 80
s','\bf(4) 64 s','\bf(5) 32 s','\bf(6) 16 s','\bf(7) 8 s')
        xlabel('\bfPixel', 'FontSize', font)
        ylabel('\bfDigital Pixel Value', 'FontSize', font)
        set(h,'XLim',[0 60])
        h = subplot(2,2,2);
        xlabel('\bfSpatial frequency (lp/mm)','FontSize', font)
        ylabel('\bfMTF', 'FontSize', font)
        set(h,'XLim',[0 10])
        h = subplot(2,2,3);
        xlabel('\bfSpatial frequency (lp/mm)', 'FontSize', font)
        ylabel('\bfNPS (mm^2)', 'FontSize', font)
        set(h,'XLim',[0 10])
        h = subplot(2,2,4);
        xlabel('\bfSpatial frequency (lp/mm)', 'FontSize', font)
        ylabel('\bfDQE', 'FontSize', font)
        set(h,'XLim',[0 4])
    end

    function NPS_parameters
        shift = 32;
        x_min = 1;
        y_min = 1;

        %Initialize variables
        roiSize = 64;
        no_of_ROI = 0;
        sumNoise = zeros(roiSize);
        sumNPS = zeros(roiSize);
        [X,Y] = meshgrid(1:roiSize, 1:roiSize);


    end

    function DQE_parameters
        A = ((effective_pixel_size/10)*roiSize).^2; %ROI area, cm^2
        power = 250;                                %kW
        phi = power*8.65e6/450;                     %neutron flux,
n/cm^2/s

        %Number of incident neutrons
        %N.(char(nameRecord(1))) = phi*A*101;
        N.(char(nameRecord(2))) = phi*A*101;
        N.(char(nameRecord(3))) = phi*A*80;
        N.(char(nameRecord(4))) = phi*A*64;
```

```
        N.(char(nameRecord(5))) = phi*A*32;
        N.(char(nameRecord(6))) = phi*A*16;
        N.(char(nameRecord(7))) = phi*A*8;

        spatial_frequency3 = 0:0.1:max(spatial_frequency);

    end

    function display_results
        NPSi, DQE_integral, MTF10
        disp('DQE:  101   80    64   32  16  8');
        disp(num2str([DQE_integral.(char(nameRecord(2)))
DQE_integral.(char(nameRecord(3))) DQE_integral.(char(nameRecord(4)))
DQE_integral.(char(nameRecord(5))) DQE_integral.(char(nameRecord(7)))
]));
        disp('NPS:  101   80    64   32  16  8');
        disp(num2str([NPSi.(char(nameRecord(2)))
NPSi.(char(nameRecord(3))) NPSi.(char(nameRecord(4)))
NPSi.(char(nameRecord(5))) NPSi.(char(nameRecord(6))),
NPSi.(char(nameRecord(7))) ]));
        disp('MTF10:  CB  101   80    64   32  16  8');
        disp(num2str([MTF10.(char(nameRecord(1)))
MTF10.(char(nameRecord(2))) MTF10.(char(nameRecord(3)))
MTF10.(char(nameRecord(4))) MTF10.(char(nameRecord(5)))
MTF10.(char(nameRecord(6))) MTF10.(char(nameRecord(7)))]));

    end
end
```